Spatial representations in macaque hippocampal formation

Dun Mao[1,2], Eric Avila[1], Baptiste Caziot[1], Jean Laurens[3], J. David Dickman[2], Dora E. Angelaki[1,2,4]*

[1]Center for Neural Science, New York University, New York, NY 10003.
[2]Department of Neuroscience, Baylor College of Medicine, Houston, TX 77030.
[3]Ernst Strüngmann Institute for Neuroscience, Frankfurt, Germany.
[4]Tandon School of Engineering, New York University, New York, NY 11201.
*Correspondence to: da93@nyu.edu.

Abstract: The hippocampal formation is linked to spatial navigation but direct evidence in primates during active, unconstrained navigation is lacking. Combined with accurate behavioral tracking of eye and head, we record neurons across hippocampal regions in rhesus macaques during free foraging in an open arena. We find that neurons encode a broad spectrum of spatial variables beyond place fields. Most neurons show mixed selectivity, with diverse representations covering the entire space. The allocentric representations are dominated by facing location and tilt orientation, and a rather low fraction of neurons shows place or grid fields. Spatial facing selectivity mainly reflects head-, rather than gaze-related, properties. These findings reveal that the macaque hippocampal formation represents space using a multiplexed code, with heading properties dominating over simple place coding during free behavior.

Main Text:

The rodent hippocampal formation (HF) has been linked to spatial navigation, and multiple cell types have been identified to encode position, head direction, and speed (*1*–*5*). Population activity tiles the entire environment (*6*, *7*), supporting the notion of a map-like representation in the rodent HF. Three-dimensional position and direction encoding has been found in the bat HF (*8*, *9*); but primate HF has been scarcely explored under the same experimental paradigms. On the one hand, human studies have been limited to virtual navigation and focused exclusively on a limited number of spatial variables, including position and direction (*10*–*13*). On the other hand, non-human primate studies have used almost exclusively head-fixed macaques, either during cart navigation (*14*, *15*) or in a virtual environment setting (*16*, *17*), and tethered animals on a linear track (*18*). Two limited investigations in freely moving new world monkeys reported location-specific hippocampal activity reminiscent of rodent place cells (*19*, *20*). A rather provocative observation is the existence, in the HF of head-fixed macaques, of putative gaze-centered spatial representations (*16*, *21*–*23*). This property, however, which may imply differences between primates and rodents, has yet to be interrogated in freely-moving primates where head movement is a critical component of natural behavior. Further, recent studies have employed multimodal models to reveal multiplexed representations in rodent HF (*24*–*26*), emphasizing the presence of mixed selectivity in the rodent navigation circuit.

To investigate how the primate HF represents space during natural, ambulatory navigation, we trained three macaques to freely forage in an open circular arena endowed with salient sensory cues (Figs. 1A and S1). Using chronically implanted

tetrodes or single electrodes (Figs. 1B,C and S2), we recorded from 599 neurons across three HF regions in both hemispheres: hippocampus (HPC, 273 neurons), entorhinal cortex (EC, 216 neurons), and subicular complex (SUB, 110 neurons) (Table S1). To accurately track the monkeys' head position and orientation, we used a marker-based approach, combined with wireless eye tracking in one of the animals (Figs. 1D,E). A broad range of spatial variables were extracted from the markers' trajectories in 3D space (Figs. 1F and S1; Methods). Overall, the monkeys' behavior covered a broad range while salient landmarks appeared to exert a strong influence (Fig. S3). Wireless eye tracking in one monkey (Fig. 1D) revealed eye-in-head movements were predominantly within the range of ±30° horizontal and ±20° vertical (Fig. S3B, bottom right panel).

Consistent with rodent studies (*27*), the activity of HF neurons was in general very sparse and the firing rates showed log-normal distribution with SUB neurons showing the least sparsity (highest average firing rates) ($p < 0.001$, Kruskal-Wallis test) (Fig. 1G). Traditional analysis methods revealed that individual HF neurons exhibited tuning to diverse spatial variables, including head height, translational speed, azimuth head direction, LFP phase, position, facing location (where the head points at), egocentric boundary, head tilt, and angular velocity (Figs. 1H,I and S4).

However, in sharp contrast to rodents (*28*), hippocampal local field potentials (LFPs) lacked a sustained oscillatory pattern in the theta band during locomotion (Fig. S5A). Rather, the power spectrum showed a local maximum around 5 Hz, whose power exhibited a small increase as a function of movement speed ($p < 0.001$, One-way ANOVA) (Figs. S5B,C). In addition, there was a prominent broad band peak around 20 Hz, which had the largest power in EC and SUB. However, the power of this beta frequency oscillation had an opposite dependence on movement speed, being the largest when the animal was near stationary ($p < 0.001$, One-way ANOVA) (Figs. S5B,C).

To quantify the simultaneous encoding of multiple variables by HF neurons, we used a cross-validated, multivariate linear-nonlinear Poisson model framework (*24*, *25*) (Fig. 2A; Methods), which is agnostic about turning curve shape and is robust to the interdependence of encoded variables (*24*). Using a forward search method, a variable was considered to be encoded by a neuron if including it significantly improved model performance ($p < 0.05$, one-sided Wilcoxon signed rank test; Methods) (Fig. S6). Thus, each cell could encode a single variable or combination of variables – or not tuned to any spatial variable at all.

The main model included 9 variables: position (Pos), facing location (FL), egocentric boundary (EB), head tilt (HT), angular velocity (AV), head height (HH), translational speed (Spd), azimuth head direction (HD), and LFP phase (Ph) (Fig. 2A). Overall, HF population exhibited rich coding schemes (Figs. 2B,C and S6), with SUB exhibiting the strongest encoding (fraction of neurons that encoded at least one of these variables: HPC: 49%, EC: 57%, SUB: 72%). We first classified neurons based on their best-encoded single variable. Across HF regions, the most frequently coded variable was not Pos but instead FL (Fig. 2D). FL was the dominant variable encoded by 22% of the neurons, as compared to Pos, which was the dominant variable in only a small fraction (5%) of HF neurons.

Most (37%) HF neurons showed conjunctive coding of multiple variables (Fig. 2B,C and S6). Mixed selectivity was ubiquitous across all HF regions (single vs. mixed selectivity, HPC: 15% vs 34%, EC: 21% vs 36%, SUB: 25% vs 47%) (Figs. 2F and S8). Taking into consideration this mixed selectivity (a single neuron encoding more than one variable), facing location was again the most prominently coded variable across all HF regions (HPC: 19%, EC: 33%, SUB: 35%) as well as across most HPC subregions (Figs. 2E and S7). By contrast to rodents and bats, a relatively small fraction encoded position across all HF regions (HPC: 7%, EC: 15%, SUB: 12%) (Fig. 2E). Notably, different HF regions carried different combinations of mixed selectivity (Figs. 2G and S8). In the HPC, facing location and egocentric boundary, as well as LFP phase and speed, were most often co-coded in the same neurons. In the EC, facing location and egocentric boundary or position were the most frequent coding pairs. Azimuth head direction (HD) was most prominently coded in the SUB (37%) with FL and Spd. Therefore, HF neurons are tuned to mixtures of navigational variables.

Spatial representations in the HF are heterogeneous. Facing location cells and head tilt cells showed diverse tuning curves with distributed preferred firing fields (Figs. 3A,B). The preferred firing fields of the FL and HT variables covered a broad space, although dominant arena cues influenced the clustering of the firing fields at certain locations (Figs. 3C,D and S9). Similarly, Place (Pos) and EB variables were also attracted to salient arena cues (Figs. 3E,F, S10 and S11). Traditional analysis showed that a small fraction of neurons exhibited the properties of place cells and grid cells in the HPC and EC, respectively (Figs. S12 and S13A,B). In fact, the proportion of identified grid cells was near chance level (n = 11/216). Regarding speed tuning, two major clusters were encountered: monotonically increasing or decreasing speed tuning curves (Figs. 3G and S14A). Although head direction was strongly biased toward the direction of the entrance/exit door, the encoded HD variable uniformly tiled the azimuth directional space (p = 0.9, Rayleigh test) (Figs. 3H and S14B). These results suggest that the spatial coding is overall heterogeneous, with facing location cells and head tilt cells mapping an entire allocentric 3D positional and directional space.

Spatial coding in rodent HF is topographically organized along the dorsal-ventral axis (*6*, *29*). In one monkey, we recorded from nearly the entire hippocampus in the right hemisphere (Figs. S2 and S15A). The monkey hippocampal rostral-caudal axis is analogous to the ventral-dorsal axis in rodents. Consistent with human fMRI studies (*30*), we observed a gradual increase in the fraction of spatially-tuned neurons and mixed selectivity along the rostral-caudal axis (Fig. S15). The caudal entorhinal cortex in macaques is homologous to the rodent medial entorhinal cortex based on its connectivity (*31*); it showed slightly weaker spatial tuning and stronger mixed selectivity than other EC subregions (Fig. S15). These results highlight the similarities as well as differences between rodents and macaques in the topography of spatial coding across HF regions.

Finally, to disambiguate the neuronal coding between head and gaze properties, we analyzed eye movement tuning by HF neurons (monkey K only). We first assessed allocentric gaze tuning. Of particular note is what was previously described as ‘spatial view’ (SV) – where the monkey looks at in the environment (*22*, *32*), a property similar to our FL variable, but referred to gaze rather than head. Combining eye-in-head

movement and 3D head orientation allowed us to disambiguate between SV and FL (Fig. 4A). Similar to head-fixed studies (*21*), a low fraction of EC neurons (9%) showed grid-like tuning for SV as revealed using traditional grid cell analysis (Fig. S13C).When fitted as a single-variable model, 11% (28/244) of HF cells were significantly tuned to SV. This percentage was higher (24%, 58/244) when using FL rather than SV (refer to where the head and gaze points at, respectively). Critically, including all head and gaze properties in the model fitting revealed that neuronal activity was predominantly driven by FL rather than SV (46 vs. 8 tuned neurons), more so in the HPC than the EC and SUB (Figs. 4B and S16). This is in contrast with previous studies in which head and gaze were not disambiguated due to head restraint (*22*, *32*). Moreover, studies in freely moving rodents failed to exclude the possibility that azimuth HD tuning may arise from gaze direction (GD). We found that azimuth directional tuning mostly reflected head but not gaze direction (15 vs. 5 tuned neurons), especially in the HPC (Figs. 4B and S16). We also examined egocentric eye (eye-in-head) tuning. Consistent with studies in head-fixed monkeys (*23*), we found neurons tuned to eye position (EP), eye velocity (EV), and saccade (Figs. 4C-E), with the entorhinal cortex showing the strongest tuning to eye position and velocity (Fig. 4F). Overall, 16% of HF neurons were sensitive to saccade (Fig. 4G). Therefore, we conclude that allocentric FL and HD tuning in the HF predominantly reflects head, but not gaze, properties; neuronal encoding of allocentric FL and egocentric EP in HF (Fig. 4H) may link the head and eye properties in spatial exploration.

In summary, the present analyses revealed novel spatial coding schemes by the hippocampal formation in freely moving macaques, dominated by head facing location and 3D head orientation, as well as egocentric boundary. Although a comparable model-based analysis with the same spatial variables has yet to be performed in rodent HF, it is possible that HF spatial tuning differs in macaques compared to rodents. We found that many macaque HF neurons form a map-like representation for where in the environment the head points at, but not where the eye looks at, and how it is orientated in 3D. Head pointing may act as the anchor for the firing fields in the HF, whereas eye movement may be used to establish a more fine-grained picture for things seen centered at that facing location; this could link the implications of the HF in spatial exploration and visual memory (*33*). Mixed, heterogeneous selectivity may be a ubiquitous property in the HF and other higher order brain regions in primates (*16*, *17*), that can also encode task-related and non-spatial information (*17*). It is likely that increasing task complexity would further increase the mixed selectivity and heterogeneity and recruit more neurons. Overall, these results have important implications for future modeling work that investigates the neural basis of spatial navigation under naturalistic settings in primates.

References:

1. J. O'Keefe, J. Dostrovsky, The hippocampus as a spatial map. Preliminary evidence from unit activity in the freely-moving rat. *Brain Research*. **34**, 171–175 (1971).
2. M. Fyhn, S. Molden, M. P. Witter, E. I. Moser, M.-B. Moser, Spatial Representation in the Entorhinal Cortex. *Science*. **305**, 1258–1264 (2004).
3. J. S. Taube, R. U. Muller, J. B. Ranck, Head-direction cells recorded from the postsubiculum in freely moving rats. I. Description and quantitative analysis. *J. Neurosci.* **10**, 420–435 (1990).
4. B. L. McNaughton, C. A. Barnes, J. O'Keefe, The contributions of position, direction, and velocity to single unit activity in the hippocampus of freely-moving rats. *Exp Brain Res*. **52**, 41–49 (1983).

5. T. Solstad, C. N. Boccara, E. Kropff, M.-B. Moser, E. I. Moser, Representation of Geometric Borders in the Entorhinal Cortex. *Science*. **322**, 1865–1868 (2008).
6. T. Hafting, M. Fyhn, S. Molden, M.-B. Moser, E. I. Moser, Microstructure of a spatial map in the entorhinal cortex. *Nature*. **436**, 801–806 (2005).
7. M. A. Wilson, B. L. McNaughton, Dynamics of the hippocampal ensemble code for space. *Science*. **261**, 1055–1058 (1993).
8. M. M. Yartsev, N. Ulanovsky, Representation of Three-Dimensional Space in the Hippocampus of Flying Bats. *Science*. **340**, 367–372 (2013).
9. A. Finkelstein, D. Derdikman, A. Rubin, J. N. Foerster, L. Las, N. Ulanovsky, Three-dimensional head-direction coding in the bat brain. *Nature*. **517**, 159–164 (2015).
10. E. A. Maguire, N. Burgess, J. G. Donnett, R. S. J. Frackowiak, C. D. Frith, J. O'Keefe, Knowing Where and Getting There: A Human Navigation Network. *Science*. **280**, 921–924 (1998).
11. A. D. Ekstrom, M. J. Kahana, J. B. Caplan, T. A. Fields, E. A. Isham, E. L. Newman, I. Fried, Cellular networks underlying human spatial navigation. *Nature*. **425**, 184–188 (2003).
12. C. F. Doeller, C. Barry, N. Burgess, Evidence for grid cells in a human memory network. *Nature*. **463**, 657–661 (2010).
13. J. Jacobs, C. T. Weidemann, J. F. Miller, A. Solway, J. F. Burke, X.-X. Wei, N. Suthana, M. R. Sperling, A. D. Sharan, I. Fried, M. J. Kahana, Direct recordings of grid-like neuronal activity in human spatial navigation. *Nature Neuroscience*. **16**, 1188–1190 (2013).
14. N. Matsumura, H. Nishijo, R. Tamura, S. Eifuku, S. Endo, T. Ono, Spatial- and Task-Dependent Neuronal Responses during Real and Virtual Translocation in the Monkey Hippocampal Formation. *J. Neurosci.* **19**, 2381–2393 (1999).
15. S. M. O'Mara, E. T. Rolls, A. Berthoz, R. P. Kesner, Neurons responding to whole-body motion in the primate hippocampus. *J. Neurosci.* **14**, 6511–6523 (1994).
16. S. Wirth, P. Baraduc, A. Planté, S. Pinède, J.-R. Duhamel, Gaze-informed, task-situated representation of space in primate hippocampus during virtual navigation. *PLOS Biology*. **15**, e2001045 (2017).
17. R. A. Gulli, L. R. Duong, B. W. Corrigan, G. Doucet, S. Williams, S. Fusi, J. C. Martinez-Trujillo, Context-dependent representations of objects and space in the primate hippocampus during virtual navigation. *Nature Neuroscience*. **23**, 103–112 (2020).
18. Y. Hazama, R. Tamura, Effects of self-locomotion on the activity of place cells in the hippocampus of a freely behaving monkey. *Neuroscience Letters*. **701**, 32–37 (2019).
19. H. S. Courellis, S. U. Nummela, M. Metke, G. W. Diehl, R. Bussell, G. Cauwenberghs, C. T. Miller, Spatial encoding in primate hippocampus during free navigation. *PLOS Biology*. **17**, e3000546 (2019).
20. N. Ludvig, H. M. Tang, B. C. Gohil, J. M. Botero, Detecting location-specific neuronal firing rate increases in the hippocampus of freely-moving monkeys. *Brain Research*. **1014**, 97–109 (2004).
21. N. J. Killian, M. J. Jutras, E. A. Buffalo, A map of visual space in the primate entorhinal cortex. *Nature*. **491**, 761–764 (2012).
22. P. Georges-François, E. T. Rolls, R. G. Robertson, Spatial View Cells in the Primate Hippocampus: Allocentric View not Head Direction or Eye Position or Place. *Cereb Cortex*. **9**, 197–212 (1999).
23. M. L. R. Meister, E. A. Buffalo, Neurons in Primate Entorhinal Cortex Represent Gaze Position in Multiple Spatial Reference Frames. *J. Neurosci.* **38**, 2430–2441 (2018).
24. K. Hardcastle, N. Maheswaranathan, S. Ganguli, L. M. Giocomo, A Multiplexed, Heterogeneous, and Adaptive Code for Navigation in Medial Entorhinal Cortex. *Neuron*. **94**, 375-387.e7 (2017).
25. J. Laurens, A. Abrego, H. Cham, B. Popeney, Y. Yu, N. Rotem, J. Aarse, E. K. Asprodini, J. D. Dickman, D. E. Angelaki, Multiplexed code of navigation variables in anterior limbic areas. *bioRxiv*, 684464 (2019).
26. D. Ledergerber, C. Battistin, J. S. Blackstad, R. J. Gardner, M. P. Witter, M.-B. Moser, Y. Roudi, E. I. Moser, *bioRxiv*, in press, doi:10.1101/2020.06.06.129221.
27. C. A. Barnes, B. L. McNaughton, S. J. Y. Mizumori, B. W. Leonard, L.-H. Lin, in *Progress in Brain Research*, J. Storm-Mathisen, J. Zimmer, O. P. Ottersen, Eds. (Elsevier, 1990; http://www.sciencedirect.com/science/article/pii/S0079612308612571), vol. 83 of *Understanding the Brain Through the Hippocampus the Hippocampal Region as a Model for Studying Brain Structure and Function*, pp. 287–300.
28. C. H. Vanderwolf, Hippocampal electrical activity and voluntary movement in the rat. *Electroencephalography and Clinical Neurophysiology*. **26**, 407–418 (1969).
29. M. W. Jung, S. I. Wiener, B. L. McNaughton, Comparison of spatial firing characteristics of units in dorsal and ventral hippocampus of the rat. *J. Neurosci.* **14**, 7347–7356 (1994).
30. E. A. Maguire, D. G. Gadian, I. S. Johnsrude, C. D. Good, J. Ashburner, R. S. Frackowiak, C. D. Frith, Navigation-related structural change in the hippocampi of taxi drivers. *Proc. Natl. Acad. Sci. U.S.A.* **97**, 4398–4403 (2000).
31. R. Insausti, D. G. Amaral, Entorhinal cortex of the monkey: IV. Topographical and laminar organization of cortical afferents. *Journal of Comparative Neurology*. **509**, 608–641 (2008).
32. E. T. Rolls, R. G. Robertson, P. Georges-François, Spatial View Cells in the Primate Hippocampus. *European Journal of Neuroscience*. **9**, 1789–1794 (1997).
33. E. T. Rolls, S. Wirth, Spatial representations in the primate hippocampus, and their functions in memory and navigation. *Prog. Neurobiol.* **171**, 90–113 (2018).
34. H. Meng, A. M. Green, J. D. Dickman, D. E. Angelaki, Pursuit—Vestibular Interactions in Brain Stem Neurons During Rotation and Translation. *Journal of Neurophysiology*. **93**, 3418–3433 (2005).
35. A. Fedorov, R. Beichel, J. Kalpathy-Cramer, J. Finet, J.-C. Fillion-Robin, S. Pujol, C. Bauer, D. Jennings, F. Fennessy, M. Sonka, J. Buatti, S. Aylward, J. V. Miller, S. Pieper, R. Kikinis, 3D Slicer as an image computing platform for the Quantitative Imaging Network. *Magnetic Resonance Imaging*. **30**, 1323–1341 (2012).
36. P. A. Yushkevich, J. Piven, H. C. Hazlett, R. G. Smith, S. Ho, J. C. Gee, G. Gerig, User-guided 3D active contour segmentation of anatomical structures: Significantly improved efficiency and reliability. *NeuroImage*. **31**, 1116–1128 (2006).
37. G. Paxinos, M. Petrides, X.-F. Huang, A. W. Toga, *The Rhesus Monkey Brain in Stereotaxic Coordinates* (Elsevier Science, 2008).
38. K. S. Saleem, N. K. Logothetis, *A Combined MRI and Histology Atlas of the Rhesus Monkey Brain in Stereotaxic Coordinates* (Elsevier, 2006).

39. N. M. Dotson, S. J. Hoffman, B. Goodell, C. M. Gray, A Large-Scale Semi-Chronic Microdrive Recording System for Non-Human Primates. *Neuron*. **96**, 769-782.e2 (2017).
40. D. E. Angelaki, J. Ng, A. M. Abrego, H. X. Cham, E. K. Asprodini, J. D. Dickman, J. Laurens, A gravity-based three-dimensional compass in the mouse brain. *Nature Communications*. **11**, 1855 (2020).
41. C. Rossant, S. N. Kadir, D. F. M. Goodman, J. Schulman, M. L. D. Hunter, A. B. Saleem, A. Grosmark, M. Belluscio, G. H. Denfield, A. S. Ecker, A. S. Tolias, S. Solomon, G. Buzsáki, M. Carandini, K. D. Harris, Spike sorting for large, dense electrode arrays. *Nature Neuroscience*. **19**, 634–641 (2016).
42. M. Haller, T. Donoghue, E. Peterson, P. Varma, P. Sebastian, R. Gao, T. Noto, R. T. Knight, A. Shestyuk, B. Voytek, Parameterizing neural power spectra. *bioRxiv*, 299859 (2018).
43. P. Berens, CircStat: A MATLAB Toolbox for Circular Statistics. *Journal of Statistical Software*. **31**, 1–21 (2009).
44. W. E. Skaggs, B. L. McNaughton, K. M. Gothard, E. J. Markus, in *In* (Morgan Kaufmann, 1993), pp. 1030–1037.
45. R. F. Langston, J. A. Ainge, J. J. Couey, C. B. Canto, T. L. Bjerknes, M. P. Witter, E. I. Moser, M.-B. Moser, Development of the Spatial Representation System in the Rat. *Science*. **328**, 1576–1580 (2010).

Acknowledgments: We thank J. Lin and B. Kim for help with setting up the arena; G. DeAngelis for help with surgeries; M. Schartner for help with the video-based tracking system; N. Tataryn for veterinary care; L. Lu and K. Bohne for advice on the tetrode technique; K. Lakshminarasimhan for help with the model fitting. **Funding:** NIH BRAIN Initiative grant U01 NS094368 and Simons Collaboration on the Global Brain Grant 542949 (D.E.A.). **Author contributions:** D.M. and D.E.A. designed the study. D.M., E.A., and B.C. set up the arena and designed the eye tracker holder. D.M., E.A., and J.D.D. performed the surgeries. D.M. trained the monkeys, performed the experiments, and analyzed the data. J.L. contributed to the analysis. D.M. and D.E.A. wrote the manuscript with inputs from all other authors. **Competing interests:** Authors declare no competing interests.

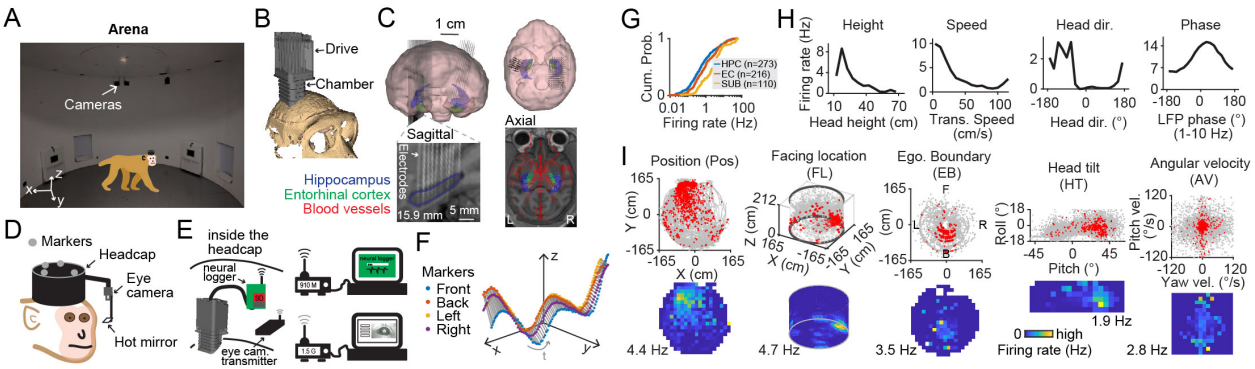

Fig. 1. Freely moving monkey setup to study spatial coding in macaque hippocampal formation during natural behaviors. (A) Monkeys were trained to freely forage for randomly scattered food pellets or fruits in an open circular arena (pictured, 330 cm diameter, 212 cm height) equipped with a motion tracking system. (B) A large-scale semi-chronic microdrive holding 124 independently movable electrodes (42 mm travel distance) was implanted in the right hemisphere of monkey K. The drive and skull models are shown. (C) Top: segmented models of the brain, where hippocampus (blue), and entorhinal cortex (green) are shown (front and top views). Bottom: recording electrodes (white lines; reconstructed from coregistered pre-op MRI and post-op CT images) for monkey K. The sagittal image is taken at 15.9 mm from midline. An axial plane superimposed with projected regions of the hippocampus, entorhinal cortex, and blood vessels is shown at bottom right. Electrodes are visible as white dots. (D) A marker-based approach was used to track head motion in 3D. Four markers were placed on the head cap. An eye tracker was attached to the head ring for tracking the pupil position of the left eye of monkey K. (E) Neural data were recorded and stored in a neural logger that was regularly synchronized with the computer. Eye tracking images were wireless transmitted online at ~30 Hz. (F) A short segment of the markers' trajectories in 3D, from which head position, translation, and orientation were extracted. (G) Cumulative distribution of the mean firing rates (over the entire sessions) for neurons recorded across three regions: hippocampus (HPC), entorhinal cortex (EC), and subicular complex (SUB). (H) Example raw tuning curves plotted as the average firing rate vs. head height, translational speed, azimuth head direction, and LFP phase (1-10 Hz). (I) Example raw data (top) and raw tuning curves (bottom) for horizontal position, facing location (where the head points at on the arena surface), egocentric boundary, head tilt, and head angular velocity. Red dots: spikes; gray: behavioral variables, down-sampled for visualization. Tuning curves (bottom) show color maps of raw firing rate (no smoothing) as a function of each behavioral variable. In each panel, the peak firing rate (yellow) is indicated with a number at the bottom of the color maps. The lowest firing rate (dark blue) is 0 for all panels. The variable abbreviations are indicated in the title for each panel in (H) and (I). Tuning curves are all from different neurons.

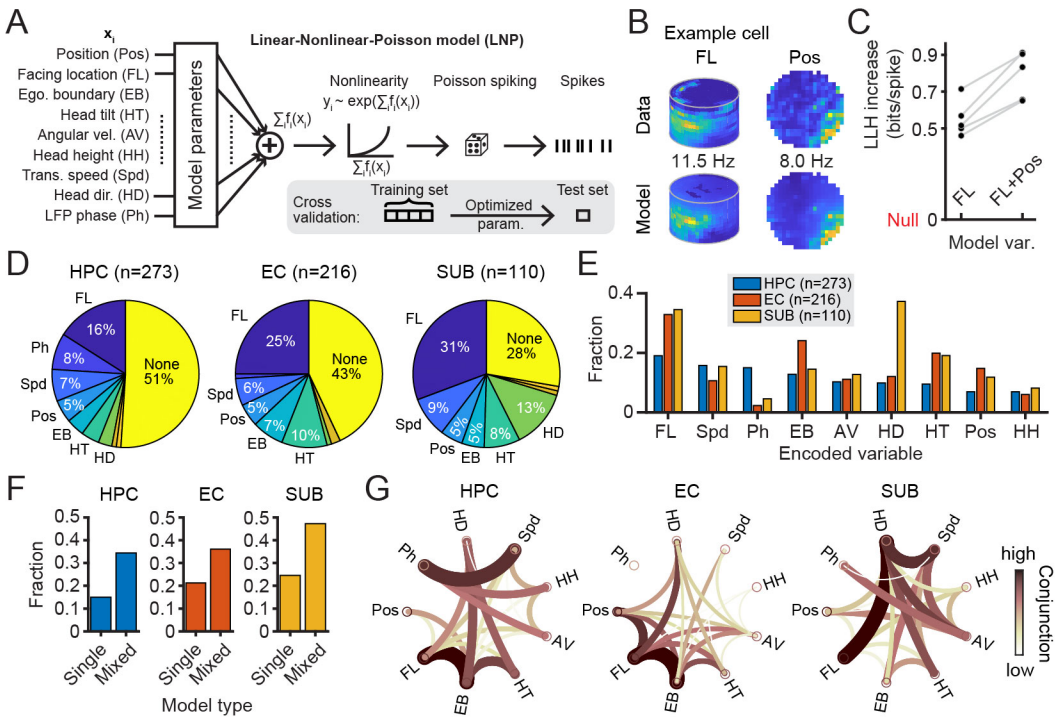

Fig. 2. Macaque hippocampal formation neurons show mixed selectivity of diverse navigational variables. (A) A model-based statistical framework was used to quantify the spatial coding. Any single variable or combination of multiple variables was fitted to the data. A forward search approach was used to select the best model. A 5-fold cross-validation was used to test the significance of the model fitting (Methods). (B) An example cell showing tuning to facing location and position. (C) Log-likelihood (LLH; goodness of fit) increase as a function of model variables for the example cell shown in (B). (D) All neurons were classified according to the single variable that best explained their responses. Pie chart shows the name and the fraction of select variables in each region. 'None' cluster corresponds to neurons that did not encode any of these variables (no spatial tuning model was better than the null model; Methods). (E) Breakdown of the fraction of encoding neurons for each variable in each region. A single neuron can encode none, one, or more than one variable. The most commonly-coded variable across regions was Facing Location (FL), with the exception of SUB, which was dominated by Head Direction (HD); Egocentric Boundary (EB) was also prominent in EC. (F) Fraction of neurons tuned to single variable (single) or to more than one variable (mixed) in each region. (G) Circular graph representation of the degree of conjunction between variables. Line thickness and color correspond to how often two variables are co-coded in a single neuron. The thicker and the darker the line, the stronger the conjunction between the two variables.

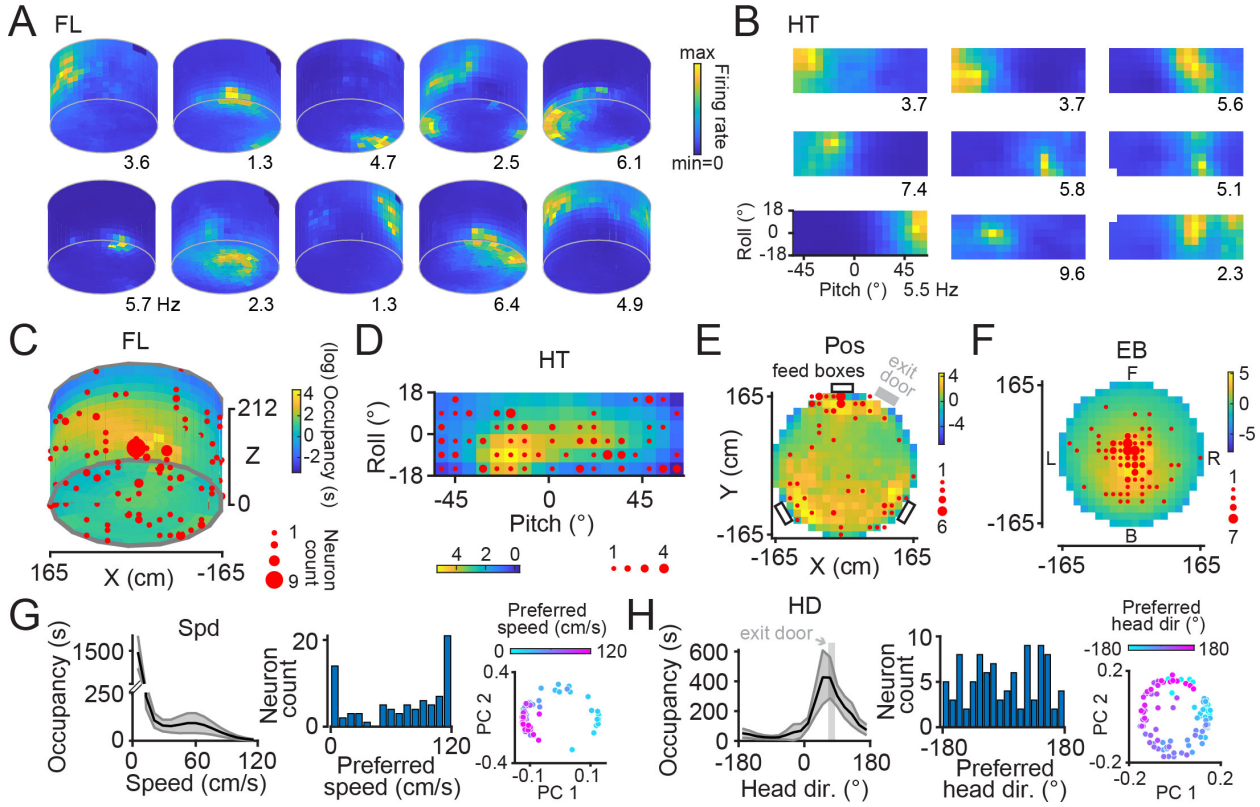

Fig. 3. Spatial representations in the hippocampal formation are heterogeneous. (A) Example model-based tuning curves for 10 neurons coding facing location (FL). Peak firing rates are indicated. Darkest blue corresponds to bins that were not occupied. (B) Example model-based tuning curves for 9 neurons that encoded head tilt (Tt). (C) Preferred firing locations (red dots) for all FL cells superimposed on the average occupancy color map (log scale) across all monkeys. Dot size corresponds to the number of neurons. (D) Preferred firing fields (red dots) for all Tt cells superimposed on the average occupancy color map (log scale) across all monkeys. Dot size corresponds to the number of neurons. (E) and (F) The same as (C) and (D) for position (Pos) encoding cells and egocentric boundary (EB) cells. Feed boxes are indicated as black rectangles. Exit/entrance door is indicated as gray rectangle in (E). (G) Average occupancy as a function of translational speed (Spd) across monkeys (left). Shaded area indicates 1x standard deviation across sessions. Distribution of preferred speed (middle). The right panel shows results of clustering analysis for the normalized speed tuning curves using principal component analysis (the first 2 components are shown). Each dot represents a single neuron. Colors correspond to their preferred speed. (H) The same as (G) for head direction (HD). Gray bar indicates the direction of the exit/entrance door.

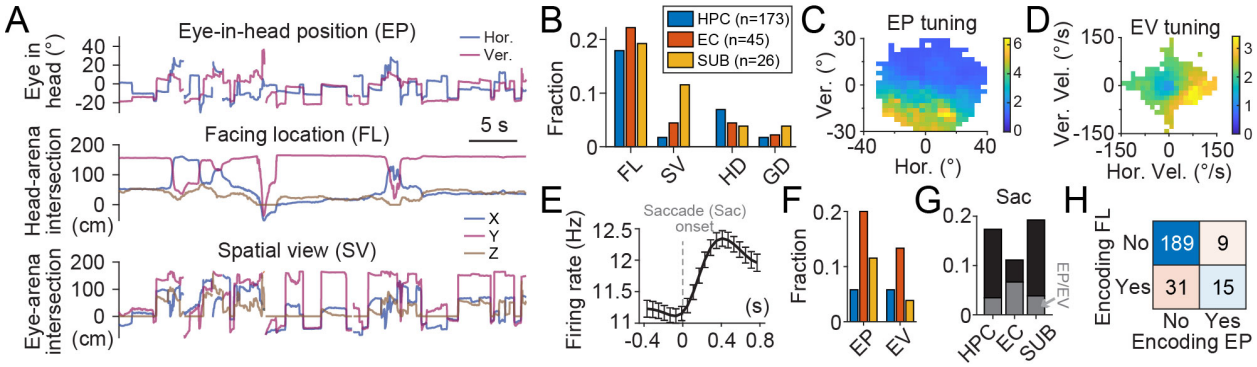

Fig. 4. Allocentric facing location and head direction tuning predominantly reflects head but not gaze properties. (A) Example raw traces showing eye-in-head position (EP, horizontal and vertical), facing location (FL), and spatial view (SV). (B) Fraction of neurons in each region encoding FL, SV, azimuth head direction (HD) and gaze direction (GD) when fitting all head- and gaze-related variables simultaneously. (C) Colormap representation of the firing as a function EP for an example tuned neuron. (D) Colormap representation of the firing as a function of eye-in-head velocity (EV) for an example tuned neuron. (E) Mean firing rate as a function of time from saccade onset for an example tuned neuron. Error bars: SEM over saccade events. (F) Fraction of neurons in each region (color-coded bars, same as (B)) encoding EP and EV when fitted as single-variable models. (G) Fraction of neurons in each region (x axis) encoding saccade event. Neurons were identified by comparing pre-saccade (-0.4-0 s) and post-saccade (0-0.4 s) activity ($p<0.01$, paired-*t* test). Overlapping neurons encoding EP or EV are shown as stacked bars. (H) Confusion matrix showing the number of neurons encoding (or not) FL and EP. Data from monkey K.

Materials and Methods

Animals

Three male rhesus macaques (*Macaca mulatta*, 8-10 years old) weighing 9-14 kg were used in this study. Monkeys B and K were both pair-housed with another male cagemate; monkey L was single-housed. Animal room was illuminated on a normal 6am-6pm 12-hr cycle. All animals were chronically implanted with a lightweight polyacetal head ring for head restraint (*34*). A head cap printed with carbon-fiber reinforced nylon (Utah Trikes, USA) was attached on the head ring to accommodate and protect the microdrives, recording devices, transmitters, and batteries. We used the standard pole-and-collar method to train the monkeys to move from their home cage to the primate chair using positive reinforcement. All animal experimental procedures and surgeries were approved by the Institutional Animal Care and Use Committee at Baylor College of Medicine and were in accordance with the National Institutes of Health guidelines.

General surgical procedures

Dexamethasone (0.5 mg/kg IM) was administered for craniotomies on the day prior to surgery and just prior to surgery in order to reduce inflammation and intracranial pressure. Monkeys were sedated using Ketamine (5-15 mg/kg, IM) with or without Dexmedetomidine (0.005-0.015 mg/kg, IM). Animals also received sustained release buprenorphine (0.2 mg/kg SC) for analgesia. Atropine (0.5 mg/kg, IM) may have been given to avoid congestion or maintain cardiac output. Sterile ophthalmic ointment was applied to the eyes to protect the corneas from drying. An intravenous catheter was placed in the saphenous vein (maintained by saline flush solution). Hair was removed at the surgical site with electric clippers. Monkeys were intubated to maintain a clear airway and placed in a stereotaxic apparatus on a surgery table. Anesthesia was maintained throughout the procedure using inhaled isoflurane (1-5%) and continuous intravenous infusion of propofol (2.5-5.0 mg/kg bolus followed by 0.3-0.4 mg/kg/hr). The level of anesthesia was monitored using withdrawal reflex, corneal reflex, jaw tone, respiration, heart rate and rhythm, blood pressure, expired CO2, O2 saturation, and mucous membrane color. Respiration was maintained using a mechanical ventilator beginning at onset of propofol infusion. Saline solution (0.9% NaCl) was infused at a rate of ~10 ml/kg/hr for the first hour followed by ~5 ml/kg/hr for the remainder of the procedure. Body temperature was maintained at ~37°C using a warm water blanket and a circulating warm air blanket. The surgical site was prepared with three alternating scrubs of povidone-iodine and sterile saline. In a separate room, two surgeons performed sterile hand scrubs and donned sterile surgical gowns and gloves. Monkeys were then covered with a sterile surgical drape. Sterility was maintained throughout the procedure. Following the procedure, monkeys were extubated after regaining the swallowing reflex and returned to the home cage once fully conscious. Monkeys were monitored until fully mobile. Antibiotics and analgesics were given as needed.

Planning for microdrive implantation

Pre-op computed tomography (CT) and magnetic resonance imaging (MRI) (3T, Siemens) images were collected to segment the regions of interest, and for accurate design of the form-fitting (to the skull) chambers (titanium) and the microdrives (form fitting to the brain surface) (Visijet-Clear or Ultem). CT and MRI images were registered in 3D slicer software (*35*) (https://www.slicer.org). The hippocampus, entorhinal cortex, subicular complex, and the entire brain were segmented semi-manually from the T1-weighted MRI images in ITK-SNAP software (*36*) (www.itksnap.org), with reference to standard atlas (*37*, *38*). Major blood vessels were

segmented from the T2-weighted MRI images. The skull model was segmented from the CT images. All rendered 3D models were exported from ITK-SNAP and then imported into 3D slicer. The MRI and CT volumes were aligned with stereotaxic coordinates in 3D slicer. Four fiducial markers were placed at the left and right infraorbital ridges and ear canals, respectively (they should be within the same plane). The stereotaxic origin is defined as the center point of left-right ear canal axis. The axial plane is parallel to the plane defined by the 4 fiducial markers. The coronal plane is perpendicular to the axial plane and parallel to the left-right ear canal axis. The sagittal plane is perpendicular to both the axial and coronal planes. Models of the chambers and microdrives were imported in 3D slicer and the best positioning was chosen such that the electrodes covered the largest extent of the hippocampus and the posterior entorhinal cortex (homolog to the medial entorhinal cortex in rodents). Major blood vessels were avoided. For monkey K, some electrodes targeted the thalamus and parietal cortex.

Preparation and implantation of chronic microdrives

Monkey K was implanted with a 32-channel Microdrive (SC32) in the left hemisphere and a 124-channel Microdrive (LS124; Gray Matter Research, LLC, USA) in the right hemisphere (*39*). Each channel was loaded with a glass-coated tungsten electrode (250 µm total diameter, 60° taper angle, ~1MΩ impedance; Alpha Omega Co., USA). Each electrode has a travel distance of 42 mm from the brain surface. The implantation procedure breaks into 3 separate surgeries (Gray Matter Research) (https://www.graymatter-research.com/documentation-manuals/): Chamber implantation, craniotomy, and microdrive implantation. In stage 1, the chamber was implanted at the desired location using C&B Metabond (Parkell, Inc., USA) and dental cement; bone anchor screws were not required since everything was protected within the head cap. The chamber was hermetically sealed with a plug and O-rings. At 10 days after stage 1, we collected fluid sample from the inside of the chamber and cultured the sample. We did not notice any sign of infection and we moved on to stage 2. In stage 2, a craniotomy was made inside the chamber and the edge of the craniotomy was polished with 90 degree rongeurs. A form-fitting plug (with the same shape as the microdrive) was installed and the plug & chamber unit was hermetically sealed. At 10 days after surgery, we controlled for infection again by collecting and culturing a fluid sample from the inside of the chamber. We did not notice sign of infection and moved on to the final stage. In stage 3, the microdrive, loaded with electrodes, was inserted into the chamber and secured to the chamber walls using multiple screws. The entire assembly was then hermetically sealed with O-rings. All components were autoclaved or gas-sterilized prior to the procedures.

Monkeys B and L were implanted with the NLX-18 and NLX-9 tetrode drives (retired product; Neuralynx, Inc., USA). We used a tetrode-in-guide tube technique. First, guide tubes (2” 27G needles) were loaded and fixed inside a grid, which rested inside a chamber. The depths of the guide tubes were planned such that they were implanted ~3-5 mm above the target regions. Second, a polymicro capillary tubing (100 µm ID, 170 µm OD; Molex, LLC, USA) was loaded into the guide tubes and glued to the drive shuttles. Third, each tetrode (Platinum 10% Iridium, 0.0007”; California Fine Wire Co., USA) was loaded into the polymicro capillary tubing. The tetrode was glued to the capillary tubing and its tip extended outside from the bottom of the tubing for ~2-3 mm. The NLX-18 drive was loaded with 16 tetrodes and the NLX-9 with 8 tetrodes. The tetrodes were plated with platinum to an impedance of 100-200 kΩ. The entire drives were gas-sterilized before surgery. Monkey B received an NLX-18 drive in the right hemisphere. Monkey L received an NLX-18 drive in the right hemisphere and an NLX-9 drive in

the left hemisphere. The assembled drive was implanted as a single unit and a single surgery was required.

Electrode advancement and reconstruction of electrode locations

For monkey K, all electrodes targeting deep structures were moved to 8 mm below brain surface on the day of microdrive implantation; electrodes targeting superficial structures were moved to 0.5-1 mm below brain surface. All deep electrodes were advanced to 2-3 mm above target areas within 5 days following recovery from the surgery. For monkeys B and L, all tetrodes were advanced to 1 mm outside of the guide tubes on the day of implantation. Electrodes were advanced by turning fine threaded screws, at a resolution of 125 µm per revolution for single electrodes and 250 µm per revolution for tetrodes. Electrodes were advanced by 50-250 µm per day and recording was performed the next day. A CT scan was performed every 2-3 months to reconstruct current electrode locations. Electrodes were visible as white tracks in the CT images (Fig. S2). CT volumes were registered with pre-op MRI volumes to visualize electrode locations in the brain. When combined with electrode advance history, electrode locations were reconstructed with good precision. Anatomical landmarks such as ventricles, white matter and electrophysiological signatures were used to further verify electrode locations.

Freely moving monkey (FMM) arena

The FMM arena consisted of an open circular enclosure with a 3.30 m diameter and a 2.12 m height, with a single entrance/exit door and a drain on the floor (Fig. S1). The enclosure was made of white composite material. Three feed/touch-screen boxes were evenly located at the perimeter of the arena. A motion capture system (Vicon Ltd, UK) consisting of 9 infrared cameras (Bonita) was mounted in the ceiling and the wall (Fig. S1), to capture the 3D position of the reflective markers placed on the monkey's head cap at a rate of ~1 kHz. Nine video cameras (CM3-U3-13Y3M 1/2" Chameleon3 Monochrome Camera, FLIR Systems, Inc., USA) were mounted in the wall to capture videos at ~30 Hz from different angles through a transparent plastic window. A wide angle camera was mounted in the center of the ceiling for surveillance. The arena was lit by an LED lamp mounted in the ceiling.

Behavioral training and tracking

Monkeys were placed on a food delayed schedule. They were fed fewer than normal biscuits (~15%) in the morning so they were encouraged to forage for treats in the arena. The remaining daily allotment of food less the amount received in the arena was fed after the monkeys were returned to the home cage after training, and supplemented with vegetables and fruits. Their weight was recorded at least 3 times a week. The monkeys were habituated to the FMM arena in a gradual manner. They were brought from their home cage to the arena in a transfer cage. They entered/exited the arena through a single door. They were trained to freely forage for randomly scattered food pellets or fruits on the floor throughout the session. Monkeys B and L also received rewards from the reward boxes with equal probability. Monkey K did not forage at the reward boxes. The monkeys were initially allowed in the arena for a duration of ~5-10 minutes per training session. The duration gradually increased to ~1 hour towards the end of the habituation phase over a period of 1-2 months. At the end of each session, the monkey was allowed to return to the transfer cage and then back to the home cage, where they received food and additional treats. Monkeys B and K were habituated to wear a wireless eye tracking device (ISCAN, Inc., USA). Monkeys were initially trained to wear a dummy eye tracking device, which could be replaced inexpensively when destroyed, in their home cage. Once they were comfortable with the device, they usually stopped interacting with it, and at that stage, they were trained to wear the eye tracking device in the FMM arena. The eye tracking device was housed

in a rigid, 3D-printed case which was fixed to the head ring implant. The device consists of a miniature infrared camera, an infrared emitter, a hot mirror, and a transmitter. The hot mirror was held rigidly in front of the left eye and the camera faced downward at about 45° relative to the mirror.

To accurately track monkey's head motion in 3D, we used a marker-based motion tracking system. Four markers were placed within a single plane on the head cap (Fig. 1D). One marker was placed in the front and one at the back. Other two markers were symmetrically placed on the left and right (closer to the back marker). The 3D position (x,y,z) of each marker was recorded (~1 kHz) in Spike2 with a data acquisition system (Power1401, CED Ltd., UK). The eye tracking device was powered by a lightweight 3.7 V Li-Po battery. Eye images were wirelessly transmitted to a receiver placed outside of the arena. Pupil position was detected online and the horizontal and vertical position was recorded (~30 Hz) in Spike2.

The marker-based motion tracking system was calibrated before use by moving the provided calibration wand throughout the entire arena space. The eye tracking camera was calibrated by training the monkey to fixate visual target arranged on a 7x5 grid (3 cm horizontal and 2 cm vertical spacing) on a hardboard placed 10-15 cm in front of the left eye, while the monkey was head fixed in a primate chair. The actual eye position in head (in degree, horizontal and vertical) was regressed against raw eye data (recorded as voltage in Spike2, using both horizontal and vertical positions in the camera scene) using two-variable polynomial regression, thus correcting potential nonlinearities along either dimension. We obtained the regression coefficients that convert any raw eye data into eye position in head in degrees (horizontal and vertical). Assume the raw eye data in horizontal and vertical positions are x_1 and x_2, actual horizontal and vertical eye positions (in degree) are h and v, respectively; regression coefficients are β_k and α_k for h and v, respectively. We solved β_k and α_k in the following equations using least squares:

$$h_i = \beta_0 + \beta_1 x_{1i} + \beta_2 x_{2i} + \beta_3 x_{1i}^2 + \beta_4 x_{2i}^2 + \beta_5 x_{1i} x_{2i} \ (i = 1,2,3, \dots, n\ holes)$$
$$v_i = \alpha_0 + \alpha_1 x_{1i} + \alpha_2 x_{2i} + \alpha_3 x_{1i}^2 + \alpha_4 x_{2i}^2 + \alpha_5 x_{1i} x_{2i} \ (i = 1,2,3, \dots, n\ holes)$$

Electrophysiological recordings

We used a 64-channel neural logger to record broadband (0.1-7000 Hz) electrophysiological signals at 32 kHz (Deuteron Technologies Ltd., Israel). The neural logger was powered by a lightweight 3.7 V Li-Po battery. The head-stage was connected to the drive connectors directly or via a 5 cm jumper cable. The head-stage utilized a preamplifier and a 16 bit analog-to-digital converter from Intan Technologies. The signal precision was 0.2 μV. Raw signals were digitized on board and stored on a 64 GB micro-SD card (SanDisk) plugged into the logger. To avoid clock drift over time, the logger was wirelessly synchronized with the computer clock every 5-10 minutes via a USB transceiver placed outside of the arena; the transceiver was connected to the Spike2 system for synchronization between behavioral data and electrophysiological recordings. Each recording session usually lasted ~20-60 minutes. For monkey K, the chamber was used as the ground. For monkeys B and L, one guide tube or a separate screw held in the skull was used as the ground.

Data analysis

All data analysis was performed using MATLAB 2019b (The MathWorks, Inc., USA).

Extraction and binning of behavioral variables

Three dimensional behavior variables were extracted from the raw marker position data. The raw marker position data were pre-processed to fill small gaps (< 1 s) which could happen occasionally. All raw data were re-sampled to 50 Hz. At any time point, assume the positons of the front, back, left and right markers in the arena are: (x_f, y_f, z_f), (x_b, y_b, z_b), (x_l, y_l, z_l), and (x_r, y_r, z_r), respectively. Assume three orthogonal unit vectors e_1, e_2, and e_3 that define the head coordinate system: e_1 points from back to front, e_2 points from right to left, and e_3 points upward. They were calculated as following:

$$e_2 = (x_l, y_l, z_l) - (x_r, y_r, z_r);\ e_2 = e_2/\|e_2\|$$
$$u = (x_f, y_f, z_f) - (x_l, y_l, z_l);\ v = (x_f, y_f, z_f) - (x_r, y_r, z_r)$$
$$e_3 = u \times v;\ e_3 = e_3/\|e_3\|;\ e_1 = e_2 \times e_3;\ e_1 = e_1/\|e_1\|$$

Three orthogonal unit vectors (*1, 0, 0*), (*0, 1, 0*), and (*0, 0, 1*) define the world coordinate system. The rotation matrix *R* from the world coordinate to the head coordinate is exactly defined as $R = [e_1; e_2; e_3]$ (Fig. S1). Assume the coordinates (in world) of the unit vectors are: $e_1 = (e_{1x}, e_{1y}, e_{1z})$, $e_2 = (e_{2x}, e_{2y}, e_{2z})$, $e_3 = (e_{3x}, e_{3y}, e_{3z})$. Proved as following (translation vector is neglected at this stage):

$$\underset{world\ coordinate}{\begin{bmatrix}1 & 0 & 0\\ 0 & 1 & 0\\ 0 & 0 & 1\end{bmatrix}} \times R = \begin{bmatrix}e_{1x} & e_{1y} & e_{1z}\\ e_{2x} & e_{2y} & e_{2z}\\ e_{3x} & e_{3y} & e_{3z}\end{bmatrix} \Rightarrow R = \underset{head\ coordinate}{\begin{bmatrix}e_{1x} & e_{1y} & e_{1z}\\ e_{2x} & e_{2y} & e_{2z}\\ e_{3x} & e_{3y} & e_{3z}\end{bmatrix}}$$

The head coordinate system was translated such that the origin aligned with the head center (defined as the projection of the head cap center onto the same axial plane as the eye center). The translation vector was measured from the MRI and CT volumes. Thus, we obtained the markers' coordinates with the origin at the head center. Head position in the world horizontal plane was calculated as the *x* and *y* components of the average coordinates across the 4 markers. Head height was defined as the *z* component (arena floor at z=0). Translational speed was calculated as the absolute displacement of the head position divided by the interval between time points (i.e. 0.02 s). Head tilt was calculated by projecting the earth gravity vector *g* = [*0, 0, -1*] onto the head coordinate system by multiplying *g* with the rotation matrix *R*. The first 2 components of the resulting vector were used as a 2D variable (corresponding to pitch and roll angles, for small head tilts) (Fig. S1). The azimuth head direction (α, corrected for head tilt) was calculated as following (*40*): We aim to rotate the vector $e_1 = (e_{1x}, e_{1y}, e_{1z})$ by a rotation matrix $Rf(v; \theta)$ converted from an axis-angle representation (using MATLAB function *vrrotvec2mat*); the axis of rotation is denoted as *v*, and the angle is denoted as θ; assume vector *u* = [*0; 0; 1*]; *n* is a unit vector perpendicular to the plane defined by vectors e_3 and *u* in the direction following the right-hand rule.

$$v = e_3 \times u = \|e_3\| \cdot \|u\| \sin(\theta)\, n;\ \theta = \sin^{-1}\|v\|$$
$$a = Rf(v;\ \theta) \times e_1;\ \alpha = \tan^{-1}\frac{a_y}{a_x}$$

Egocentric boundary was first defined in a polar coordinate system, in which the angle is between the arena center-to-head center vector and the azimuth head direction (-180°, 180°] (negative if the boundary is on the right side of the animal); the distance is calculated as distance from the head center to nearest arena boundary (i.e. arena radius minus arena center-to-head center distance). The polar system was rotated for 90° such that +x axis points upward (when the arena boundary is in front of the animal) and +y axis points left (when the arena

boundary is on the left of the animal). The polar coordinates were converted to Cartesian coordinates, resulting in *x, y* ∈ [-165, 165] cm. To calculate the yaw, pitch, and roll angular velocity, assume the rotation matrix (i.e. the coordinates of the 3 orthogonal unit vectors that define the head coordinate system) from the world to the head is R_t and R_{t-1} at time points *t* and *t-1*, respectively; assume in the head coordinate system the rotation matrix from *t-1* to *t* is R_o; denote the rotation angles in yaw, pitch, and roll are *ψ, θ*, and *Φ*, respectively.

$$R_{t-1}{}^T \times R_o = R_t{}^T \; ; \; solve \; R_o$$

$$R_o = \begin{bmatrix} R_{11} & R_{12} & R_{13} \\ R_{21} & R_{22} & R_{23} \\ R_{31} & R_{32} & R_{33} \end{bmatrix}$$

$$given: R_o = R_z(\psi)R_y(\theta)R_x(\Phi) = \begin{bmatrix} \cos\psi & -\sin\psi & 0 \\ \sin\psi & \cos\psi & 0 \\ 0 & 0 & 1 \end{bmatrix} \begin{bmatrix} \cos\theta & 0 & \sin\theta \\ 0 & 1 & 0 \\ -\sin\theta & 0 & \cos\theta \end{bmatrix} \begin{bmatrix} 1 & 0 & 0 \\ 0 & \cos\Phi & -\sin\Phi \\ 0 & \sin\Phi & \cos\Phi \end{bmatrix}$$

$$R_o = \begin{bmatrix} \cos\psi\cos\theta & \cos\psi\sin\theta\sin\Phi - \sin\psi\cos\Phi & \cos\psi\sin\theta\cos\Phi + \sin\psi\sin\Phi \\ \sin\psi\cos\theta & \sin\psi\sin\theta\sin\Phi + \cos\psi\cos\Phi & \sin\psi\sin\theta\cos\Phi - \cos\psi\sin\Phi \\ -\sin\theta & \cos\theta\sin\Phi & \cos\theta\cos\Phi \end{bmatrix}$$

$$\frac{R_{21}}{R_{11}} = \frac{\sin\psi\cos\theta}{\cos\psi\cos\theta} = \tan\psi \Rightarrow \psi = \tan^{-1}\frac{R_{21}}{R_{11}}$$

$$R_{31} = -\sin\theta \Rightarrow \theta = \sin^{-1}(-R_{31})$$

$$\frac{R_{32}}{R_{33}} = \frac{\cos\theta\sin\Phi}{\cos\theta\cos\Phi} = \tan\Phi \Rightarrow \Phi = \tan^{-1}\frac{R_{32}}{R_{33}}$$

Computing Euler angles from the rotation matrix (https://www.gregslabaugh.net/publications/euler.pdf), we solved *ψ*, *θ*, and *Φ*, whose derivatives over time (0.02 s step) yielded the angular velocity. We focused on the yaw and pitch angular speed (as a 2D variable) only since the head rotated mostly along these 2 dimensions.

To calculate where the monkey looked at, first the eye-in-head vector was converted to the world coordinate system by multiplying it by the transpose of the rotation matrix *R*, obtaining the view vector in world. The inner surface of the arena was treated as an enclosed cylinder, composed of three surfaces: the ceiling, the floor, and the cylinder wall. We solved the intersection between the viewing vector and the three surfaces to obtain the viewing location in 3D, i.e. spatial view variable. Similarly, we calculated the intersection between the heading vector and the three planes to obtain where the head pointed at in the arena at each time point, i.e. facing location variable.

So far, we extracted 10 behavioral variables. We binned them in the following way: position (2D variable; *x, y* ∈ [-165, 165] cm; 20 x 20 bins); facing location and spatial view (3D variable; *x, y* ∈ [-165, 165] cm, *z* ∈ [0, 212] cm; 17 x 17 bins for the ceiling and floor, 53 x 11 bins for the wall); egocentric boundary (2D variable; *x, y* ∈ [-165, 165] cm; 20 x 20 bins); head tilt (2D variable; *p* ∈ [-0.8, 1], *r* ∈ [-0.3, 0.3]; 18 x 6 bins); angular velocity (2D variable; *ψ'*, *θ'* ∈ [-120, 120] °/s; 16 x 16 bins); head height (1D variable, *h* ∈ [10, 70] cm; 12 bins); translational speed (1D variable, *v* ∈ [0, 120] cm/s; 15 bins); azimuth head direction (1D circular variable, *hd* ∈ [-180, 180] °; 18 bins); LFP phase (1D circular variable, 1-10 Hz, *ph* ∈ [-180, 180] °; 18 bins).

The sampling rate was 50 Hz, i.e. 0.02 s interval. Note the position bins were empty at the 4 corners (no occupancy at those bins): This does not affect the model fitting or the evaluation of the model's performance. Sessions in which the monkeys occupied fewer than 80% of the valid position bins were excluded from further analysis.

Preprocessing of electrophysiological data

We used a semi-automatic procedure for the preprocessing of the electrophysiological data. We used the established pipelines, using the software Klusta for spike detection and automatic spike sorting and phy Kwik-Gui for manual curation (*41*). Raw data were high-pass filtered at 300 Hz for spike detection. Detection threshold was set at 5 x standard deviation. Extracted spike waveforms were aligned at trough and 0.5 ms and 1 ms of samples before and after the trough were kept for spike sorting. Automatic spike sorting results were imported in phy Kwik-Gui for manual correction using a graphical user interface. Manual corrections were based on spike waveforms, waveform features, auto-correlograms, and cross-correlograms. Only well isolated units were kept for further analysis. To obtain the LFPs, the raw data were low-pass filtered at 300 Hz and down-sampled to 1000 Hz.

LNP model fitting

To quantify the encoding of the behavioral variables by neuronal activity, we adapted a multi-predictor Linear-Nonlinear Poisson (LNP) model framework, which has been successfully used in investigating the neuronal encoding of navigational variables in the rodent hippocampal formation (*24–26*). The MATLAB code is available on GitHub (https://github.com/kaushik-l/neuroGAM). One of the major differences of the present LNP model from the conventional Poisson Generalized Linear Model (GLM) is that it takes into consideration the combinational effect/interdependence of multiple predictors on a response instead of a single predictor.

Spike trains were binned into 0.02 s time bins, the same as the behavioral variables. We obtained the measured spike train r (spike count in each time bin). Each behavioral variable x_i was represented in a one-hot matrix format X_i, in which the row corresponds to the time points (N) and the column corresponds to the binned variable (total number of bins; linearized vertically for 2D variables). The bin the monkey occupies at each time point was set to 1 while the others were all set to 0. The sum of each row is 1. The combination of one-hot matrix from different variables was achieved by concatenating each variable's one-hot matrix along the row dimension, denoted as X. To test for the significance of the model fitting and to control for overfitting, we used a 5-fold cross-validation. To obtain the training and test set with minimized bias, the data were divided into 3 chunks; in each chunk, the data were further divided into 5 sub-chunks; for each fold during the cross-validation process, the i^{th} ($i \in (1,2,3,4,5)$, 5 folds) sub-chunk in each chunk was concatenated and used as the test set (20% of data) and the remaining used as the training set (80% of data). The measured spike train r was smoothed with a Gaussian kernel with 0.06 s (3 time bins) standard deviation. For each fold, we aim to estimate the spike train r_e in the training set as a generic nonlinear (here, exponential) function of the parameterized variables:

$$r_e = e^{\sum_i X_i \omega_i} \qquad (1)$$

X is the one-hot representation of one variable or any combination of the variables (e.g. position & tilt, egocentric boundary & translational speed & LFP phase, etc; each variable denoted as X_i). ω_i is the parameter (a column vector containing one value for each bin) for the

corresponding variable. The goal is to solve ω to maximize the likelihood of observing the true spike train *r* given the estimated spike train r_e under the prior knowledge of certain model parameters (smoothness).

$$\hat{\omega} = \sum_t P(r_t|r_{e,t})P(\omega) \quad (2)$$

$$P(\omega) = \prod_i \prod_j e^{-0.5\lambda_i(\omega_{i,j}-\omega_{i,j+1})^2} \quad (3)$$

Where *j* indexes over bins and λ_i is the regularizing hyperparameter (we used 8, 4, 8, 15, 10, 50, 50, 50, 50 for position, facing location/spatial view, egocentric boundary, head tilt, angular velocity, head height, translational speed, azimuth head direction, and LFP phase, respectively) (*24*). To ease the computation, we used the log-link function, combining (1)(2)(3), the problem became:

$$\hat{\omega} = \underset{\omega}{\operatorname{argmax}} \left(\sum_t log\, P\left(r_t|e^{\sum_i X_{i,t}\omega_i}\right) - \sum_i 0.5\lambda_i \sum_j (\omega_{i,j} - \omega_{i,j+1})^2 \right)$$

The best-fit parameter was solved using the MATLAB fminunc function (using the 'trust-region' algorithm). The obtained parameter was then used to predict the spike train in the test set using equation (1). We used log-likelihood as the quantification for model performance (i.e. goodness of fit). The model performance was compared to a null model (mean firing rate model) to test if the model performance was above chance (one-sided Wilcoxon signed rank test, alpha = 0.05). The model-derived, marginalized tuning curve for each variable was calculated as following (converted to firing rate):

$$y = e^{\left(\hat{\omega}+\sum_i\sum_{k\neq i}\hat{\omega}(k,j)P(x_{k,j}=1)\right)}/0.02$$

Where *j* indexes over bins and $P(x_{kj}=1)$ is the occupancy probability in each bin.

We used an optimized forward search approach to select the best simplest model. First, we fitted the 1st order models that contained only one variable. Second, if any of the 1st order models performed better than the null model, we fitted the 2nd order models (2 variables) which included the best 1st model variable (with the highest, significant log-likelihood value). Higher order models containing the best, significant lower model variables were fitted further until the model performance did not improve. The best simplest model was selected as the final best model.

The neuron categorization (Fig. 3A) was based on the best 1st order model; for example, if the 1st order model containing the position variable has the best significant performance, this neuron is categorized as a 'position' cell. The fraction of neurons encoding each variable (Fig. 2H) was based on the final best model, in which a single neuron could encode more than 1 variable; for example, if the best model is based on egocentric boundary + translational speed + LFP phase, then this neuron is counted as encoding all these 3 variables. This approach avoided assigning variables that were significant in the 1st order models but were not picked up by the final best model since the behavioral variables could be interdependent, which is usually not taken into consideration in traditional analysis.

LFP analysis

We used the continuous wavelet transform (CWT) to compute the spectrogram. We then used a model-based approach to compute the aperiodic as well as the oscillatory components in the power spectrum (*42*) (https://github.com/fooof-tools/fooof).

To extract LFP phase, we first band-pass filtered the raw LFP to 1-10 Hz using 4th-order Chebyshev Type II filter. We then used Hilbert transform to extract instantaneous LFP phase.

Circular graph for conjunctive coding

The circular graph in Fig. 3D was plotted using code here (https://github.com/paul-kassebaum-mathworks/circularGraph). Given two logical vectors (A and B for variables x and y, respectively) in which TRUE indicates the variable is encoded by the corresponding neuron, we calculated the Jaccard index:

$$J(A,B) = \frac{|A \cap B|}{|A| + |B| - |A \cap B|}$$

Where $|A \cap B|$ indicates the neuron count that encodes both variables, $|A|$ and $|B|$ indicate neuron count encoding variable x and y, respectively. Variable pair which had a Jaccard index below 0.1 was not plotted in Fig. 3D.

Tuning curve classification

Tuning curve classification was based on the mode-derived tuning curves. We first normalized the tuning curves so that they ranged from 0 to 1. We performed principal components analysis on the correlation matrix of all tuning curves. The first two principal components were plotted in Fig. 4. See (https://github.com/PeyracheLab/Class-Decoding) for a tutorial script.

Uniformity test for data in Fig. 4H used Rayleigh test in the CircStat toolbox (*43*) (http://bethgelab.org/software/circstat/).

Traditional tuning curve-based analysis

We used the traditional methods to identify place cells based on spatial information. We compared the actual spatial information with the shuffled distributions to obtain significance. First, we constructed the position activity map (firing rate as a function of position) using 3x3 cm binning (110x110 bins for x and y). The position activity map was smoothed using a 2D Gaussian kernel with 6 cm standard deviation along each dimension. Spatial information (*SI*) was calculated using the following formula ***(44)***:

$$\boldsymbol{SI = \sum_{i=1}^{N} p_i \frac{f_i}{f} log_2 \frac{f_i}{f}}$$

where *N* is the total number of bins (110x110); p_i is the occupancy probability in the i^{th} bin; f_i is the firing rate in the i^{th} bin; *f* is the overall summed firing rate across all bins. To obtain the shuffled *SI* distributions, we circularly shifted the spike trains relative to the behavioral data for a random interval from 10 to session duration less 10 seconds, and re-calculated the *SI*. We repeated this process for 1000 times and obtained the *SI* distributions. If the raw *SI* is larger than 0.5 and it is larger than 95th percentile of the shuffled *SI*, the neuron was considered carrying significant spatial information. We performed this analysis for all HPC neurons.

Traditional methods to identify grid cells are based on comparing grid scores between actual data and shuffled distributions. We performed this grid score-based analysis for position, spatial view (floor and wall), and facing location (floor and wall), for all EC neurons. First, we computed the position activity map (floor) using 3x3 cm binning (110x110 bins), smoothed with a 2D Gaussian kernel with 6 cm standard deviation along each dimension. We computed the firing rate map on the wall using 500x100 bins (perimeter x height), smoothed with a 2D Gaussian kernel of 5x1 bins (~10.4x2.1 cm) standard

deviation along each dimension. We calculated the auto-correlogram of the position activity map $\lambda(x,y)$ as following (***45***):

$$r(\tau_x, \tau_y) = \frac{n\sum \lambda(x,y)\lambda(x-\tau_x, y-\tau_y) - \sum \lambda(x,y)\sum \lambda(x-\tau_x, y-\tau_y)}{\sqrt{n\sum \lambda(x,y)^2 - (\sum \lambda(x,y))^2}\sqrt{n\sum \lambda(x-\tau_x, y-\tau_y)^2 - (\sum \lambda(x-\tau_x, y-\tau_y))^2}}$$

This can be implemented using the Matlab imfilter function. τ_x and τ_y are the spatial shifts (in number of bins) along each dimension. The correlations for 2 position activity maps with overlapping less than 20 bins were not calculated. The correlation of the central peak of the obtained 2D auto-correlogram equals 1. We then took a circular sample of the auto-correlogram, centered at the central peak (excluded), and correlated (Pearson correlation) it with its rotated version (30°, 60°, 90°, 120°, 150°). Grid score was defined as the minimum correlation difference between any of the (60°, 120°) rotations and any of the (30°, 90°, 150°) rotations. An example script can be found here (https://github.com/robmok/code_gridCell). We obtained the shuffled distributions by circularly shifting the spike trains relative to the behavioral data for a random interval from 10 to session duration less 10 seconds, and re-calculated grid score. We repeated this process for 1000 times. Actual grid score was compared against the shuffled distributions. A neuron was considered showing significant gridness if the actual grid score is larger than 95th percentile of the shuffled distributions (either on the floor or on the wall; we also performed this grid tuning analysis on the wall for spatial view and facing location variables).

Eye movement tuning analysis

We used a speed threshold of 150 °/s to detect saccade event in either horizontal or vertical eye movement. We fitted eye position (2D variable; $x \in$ [-40, 40]°, $y \in$ [-30, 30]°; 20 x 20 bins) and eye velocity (2D variable; $x, y \in$ (-150, 150)°/s; 20 x 20 bins) in head to the LNP model (single variable model) to identify neuron tuned to either of these two variables. To identify neurons that were tuned to saccade events, we identified neurons that showed significant differences between pre-saccade and post saccade activity across saccade events (0.4 s before and 0.4 s after saccade onset; paired *t*-test, alpha = 0.01).

All p values smaller than 0.001 were indicated as $p < 0.001$; otherwise exact p values were indicated.

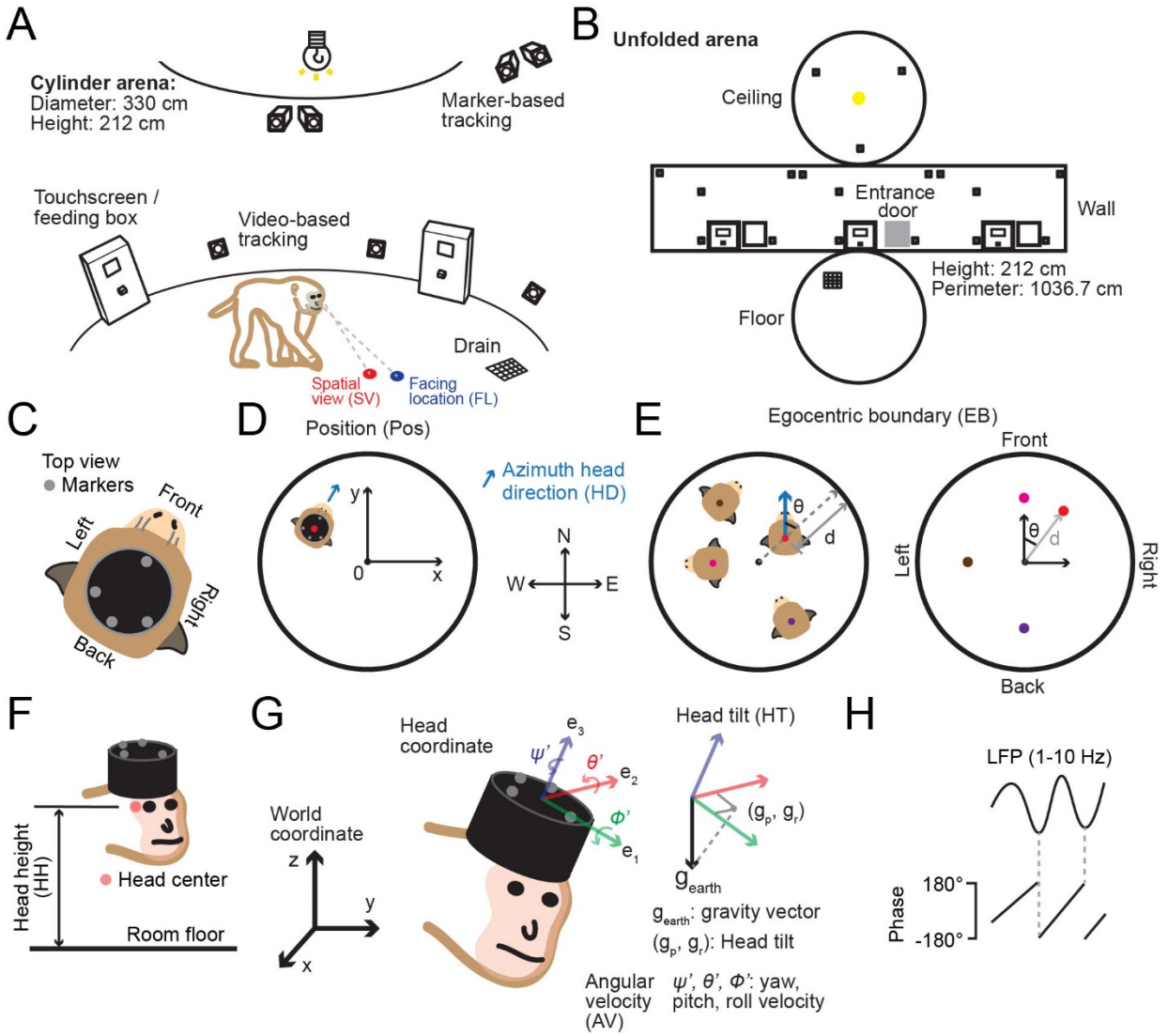

Fig. S1. Experimental setup and behavioral variables. (A) Diagram of circular arena (diameter: 330 cm; height: 212 cm), lit by a ceiling LED light, with touchscreen/feed boxes and drain as landmarks. Nine marker-based and 9 video-based tracking cameras were placed on wall and ceiling. Monkeys entered/exited the arena through a sliding door. The ***Facing location (FL)*** variable was defined as the intersection between the heading vector (where the head points at) and the arena (blue blob on the floor). The ***Spatial view (SV)*** variable was defined as the intersection between the viewing (gaze) vector (where the left eye looks at) and the arena (red blob). **(B)** Unfolded arena diagram used to define FL and SV tuning curves. **(C)** Top view of monkey head cap with 4 reflective markers for motion tracking. **(D)** ***Position (Pos)*** and **Azimuth head direction (HD)** were defined as the position/direction of the head in world coordinates (red dot/blue arrow). **(E)** ***Egocentric boundary (EB)*** was defined as the monkey's distance (d) and angle (θ) relative to the closest point of the arena boundary, shown from allocentric (left) and egocentric (right) perspectives. Magenta/gray/blue dot: boundary in front (θ = 0°)/left (θ = 90°)/back (θ = 180°) of the animal. **(F)*** **Head height (HH)***, defined as the height of the head center (red dot) from the arena floor. **(G)** ***Head tilt (HT),*** defined as the projection of the gravity vector (g_{earth}) onto the head axial plane, with components (g_p, g_r) corresponding to pitch and roll (thus, a 2D variable). ***Head angular velocity*** (yaw, pitch, and roll) was extracted from instantaneous head orientation. ***(H) Local-field potential phase***, extracted from band-pass filtered LFP (1-10 Hz), with troughs correspond to ±180°.

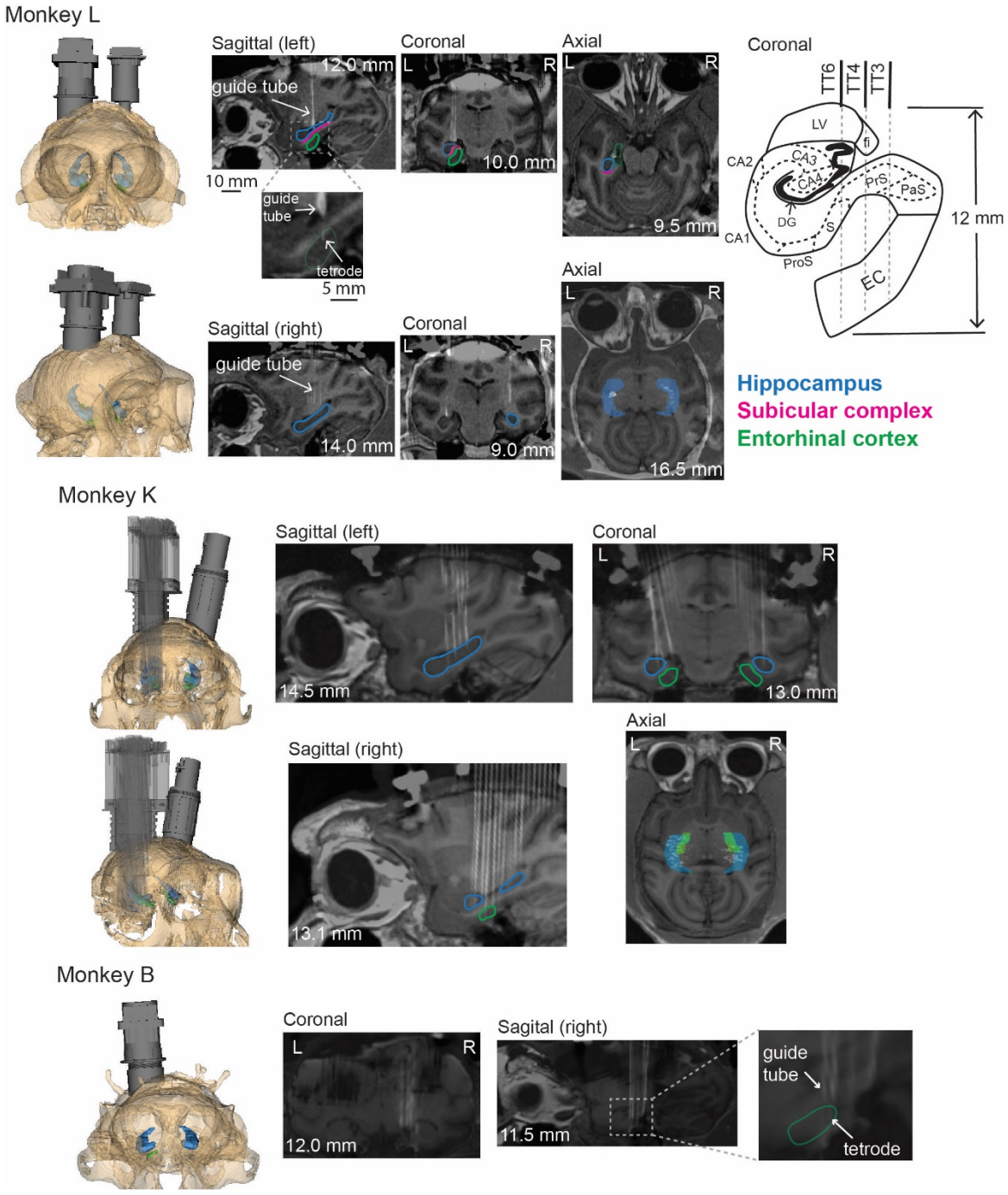

Fig. S2. Microdrive implants and reconstruction of electrode locations. Left: microdrive (gray) and skull (bone white) models for all three monkeys. Right: MRI and CT co-registered images show electrode locations as white tracks. Hippocampus: light blue; Entorhinal cortex: green; Subicular complex: magenta. Tetrodes were used for monkeys L and B; single electrodes were used for monkey K.

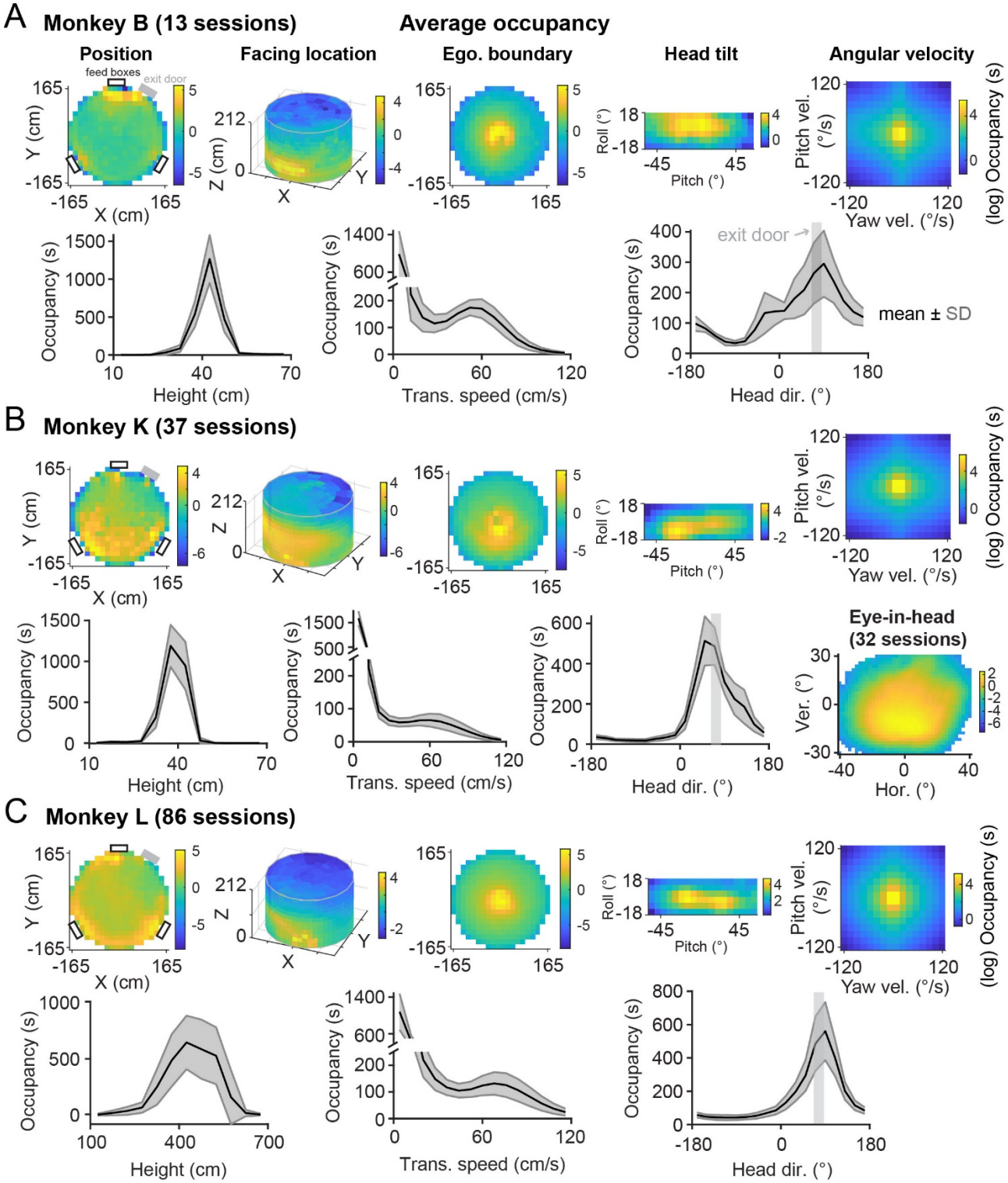

Fig. S3. Average occupancy maps for all behavioral variables. For 2D variables (from left to right: Position, Head facing location, Egocentric boundary, Head tilt, Head angular velocity, and eye-in-head position in **(B)** lower right), color indicates average time spent in each bin in natural logarithmic scale of seconds . Open rectangles: touchscreen/feed box locations. Gray rectangles: entrance/exit door location. For 1D variables (from left to right: Head height, Speed, Azimuth Head Direction), shaded area corresponds to 1x standard deviation across sessions.

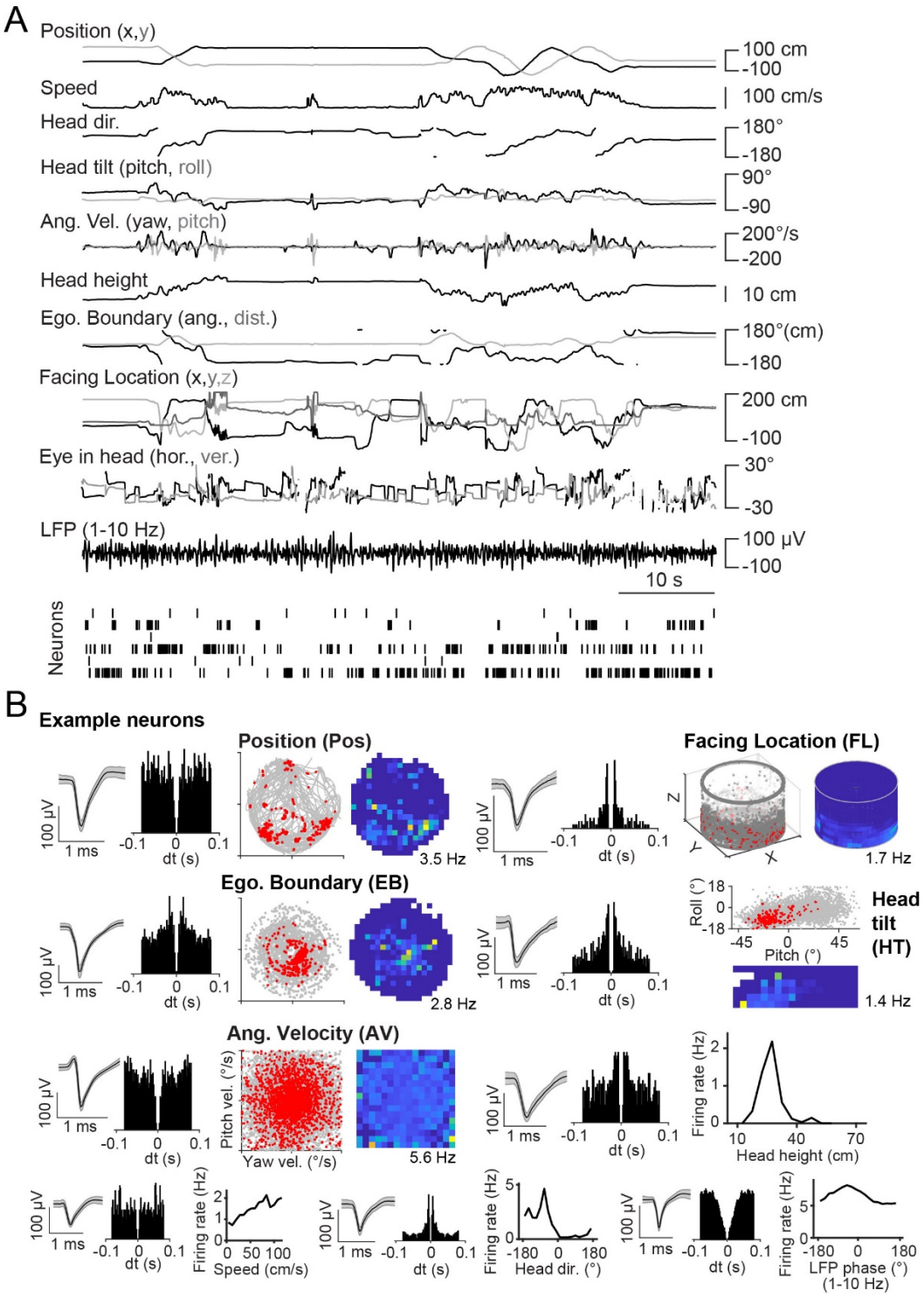

Fig. S4. Example behavioral variable traces and example raw tuning curves. (A) A short segment of the raw traces of all behavioral variables and the corresponding spike raster at the bottom. **(B)** Example neurons (from different sessions) with their raw tuning curves for the corresponding variable. Left: Average spike waveform is shown (shaded area: 1x standard deviation). Middle left: Auto-correlogram. Middle right/right: For 2D variables, down-sampled (for visualization purposes) behavioral data are shown as gray traces with superimposed spikes (red dots). Raw firing color map is also shown (no smoothing). For 1D variables, 1D tuning curves are shown instead.

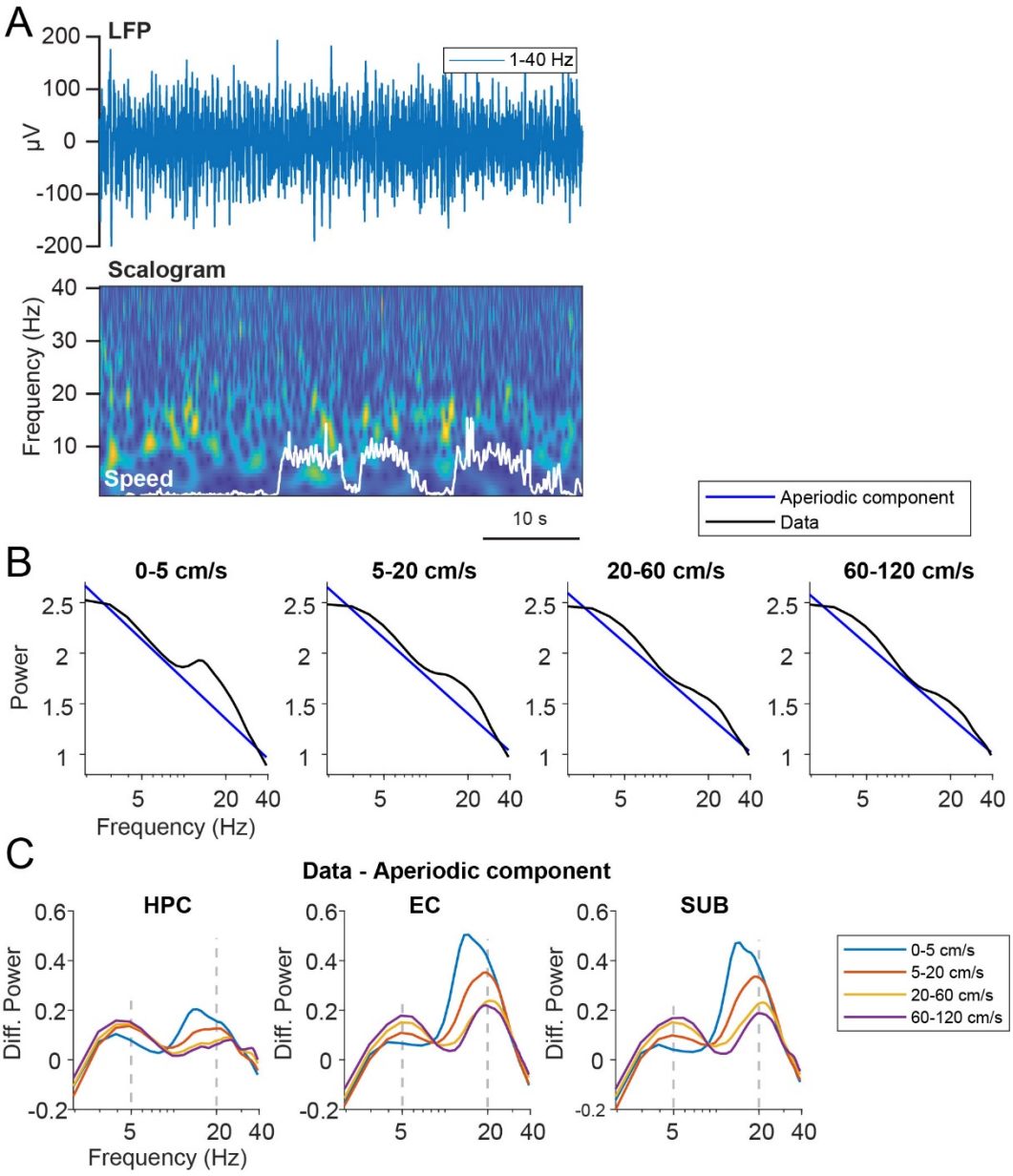

Fig. S5. LFP signature in the HF of freely moving macaques. (A) Top: example trace of raw LFP (1-40 Hz) in the hippocampus. Bottom: corresponding LFP spectrogram (scalogram) computed using continuous wavelet transform. Speed trace is also shown (white). **(B)** Average power spectrum across HF regions for different speed ranges. Actual data is shown in black. Model-fitted aperiodic component is shown in blue. **(C)** Average power spectrum for the oscillatory component (data - aperiodic component) for individual HF regions, color-coded for different speed ranges. X axis is shown in logarithmic scales for **(B)** and **(C)**. Average power between 4-6 Hz across regions as a function of speed range (0-5, 5-20, 20-60, and 60-120 cm/s): 0.07, 0.11, 0.14, and 0.16; between 18.5-21.5 Hz: 0.29, 0.24, 0.16, and 0.14.

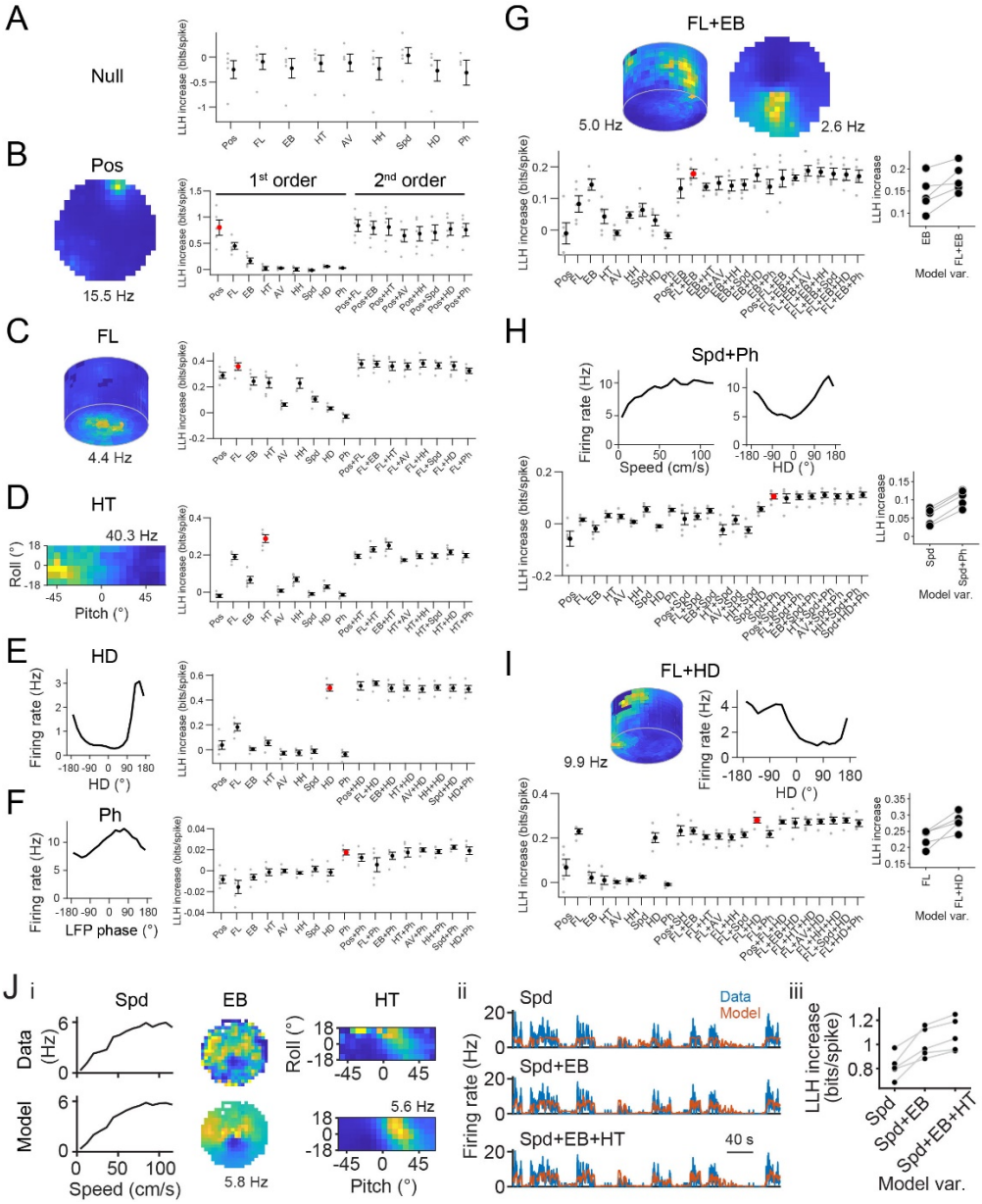

Fig. S6. Example model-based tuning curves and model selection. A forward search approach was used to identify the best model. Black dots: increase of the mean log-likelihood (LLH) (from the null, mean firing rate model). LLH increase not significantly larger than 0 indicates that the current model does not perform better than a (mean firing rate) null model. Red dot: best model selected. **(A)** An example neuron not tuned to any variable. All the LLH values of the single-variable (1st order) models are not significantly larger than 0. **(B-F)** Example neurons tuned to a single variable, with model-based tuning curves shown on the left. Examples tuned to position (Pos), facing location (FL), head tilt (HT), azimuth head direction (HD), and LFP phase. **(G-I)** Example neurons tuned to combination of 2 variables, with model-based tuning curves shown at the top. Examples tuned to FL+EB, Spd + LFP phase, and FL+HD. **(J)** An example neuron whose activity was best fitted by a 3rd-order model: the combination of speed, egocentric boundary, and head tilt. (i) Top row, raw tuning curves. Bottom row, model-based tuning curves. Peak firing rates of the color maps are indicated (lowest was 0). (ii) Actual (blue) and fitted (orange) firing rate shown for a short segment for models with different combinations of the three variables. (iii) LLH increase as a function of coded variables. Each line corresponds to one fold in the cross-validation process. Error bars: standard error over the 5 folds in cross-validation.

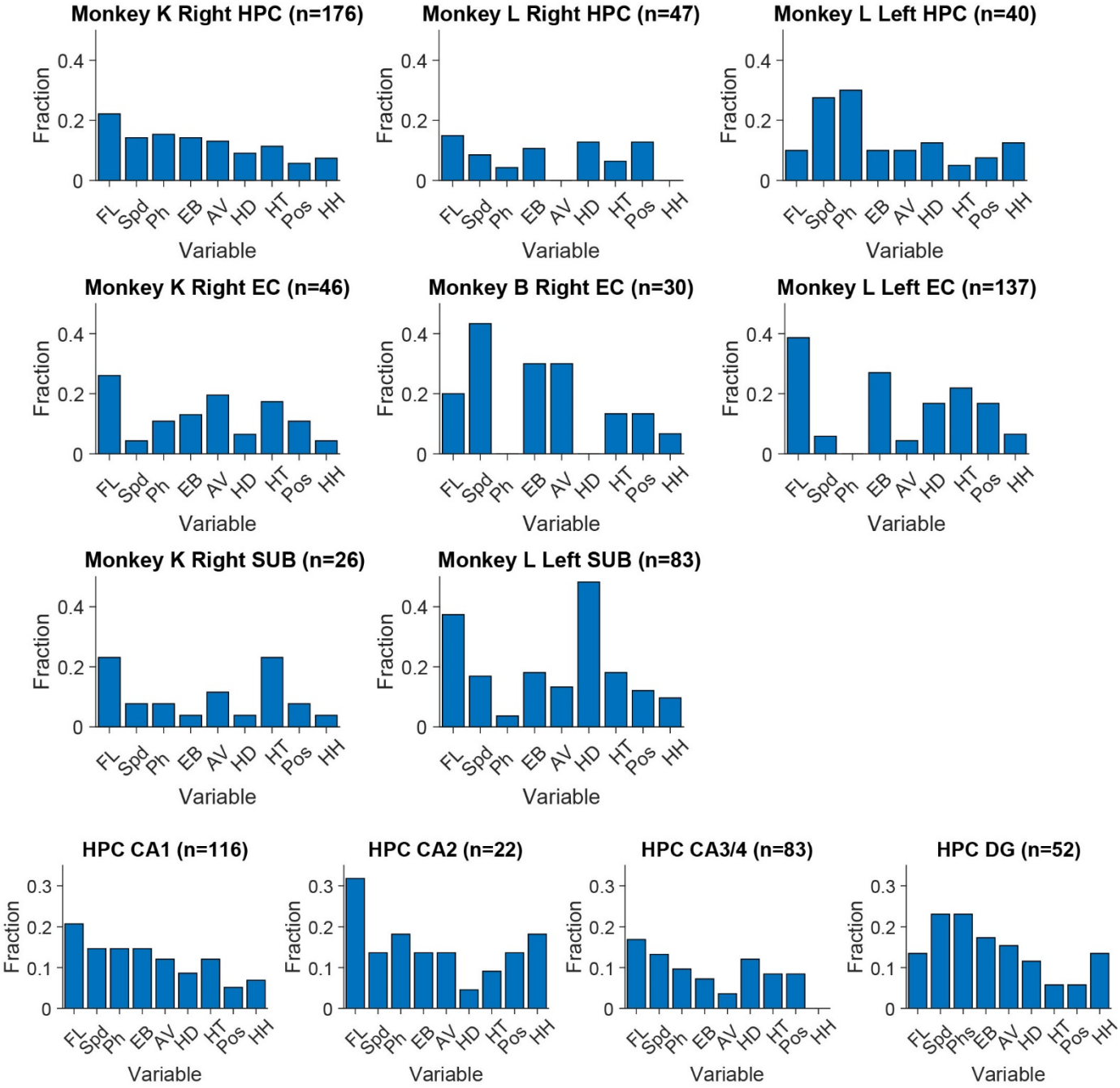

Fig. S7. Breakdown of the fraction of neurons encoding each variable into individual regions, hemispheres, monkeys, and hippocampal subregions.

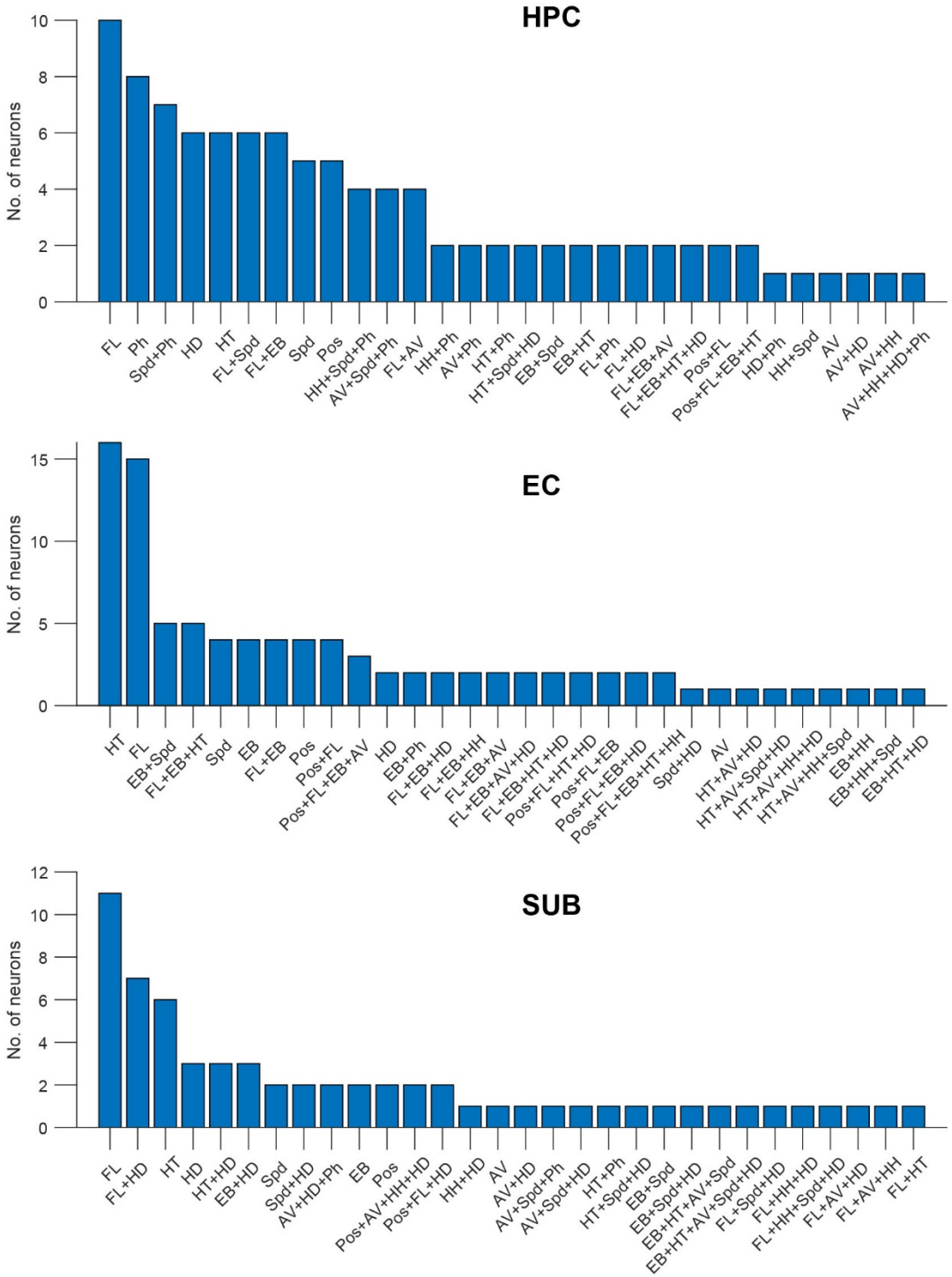

Fig. S8. Bar plots showing the number of neurons captured by the top 30 best models in each region. The best model variables are indicated as the X tick labels.

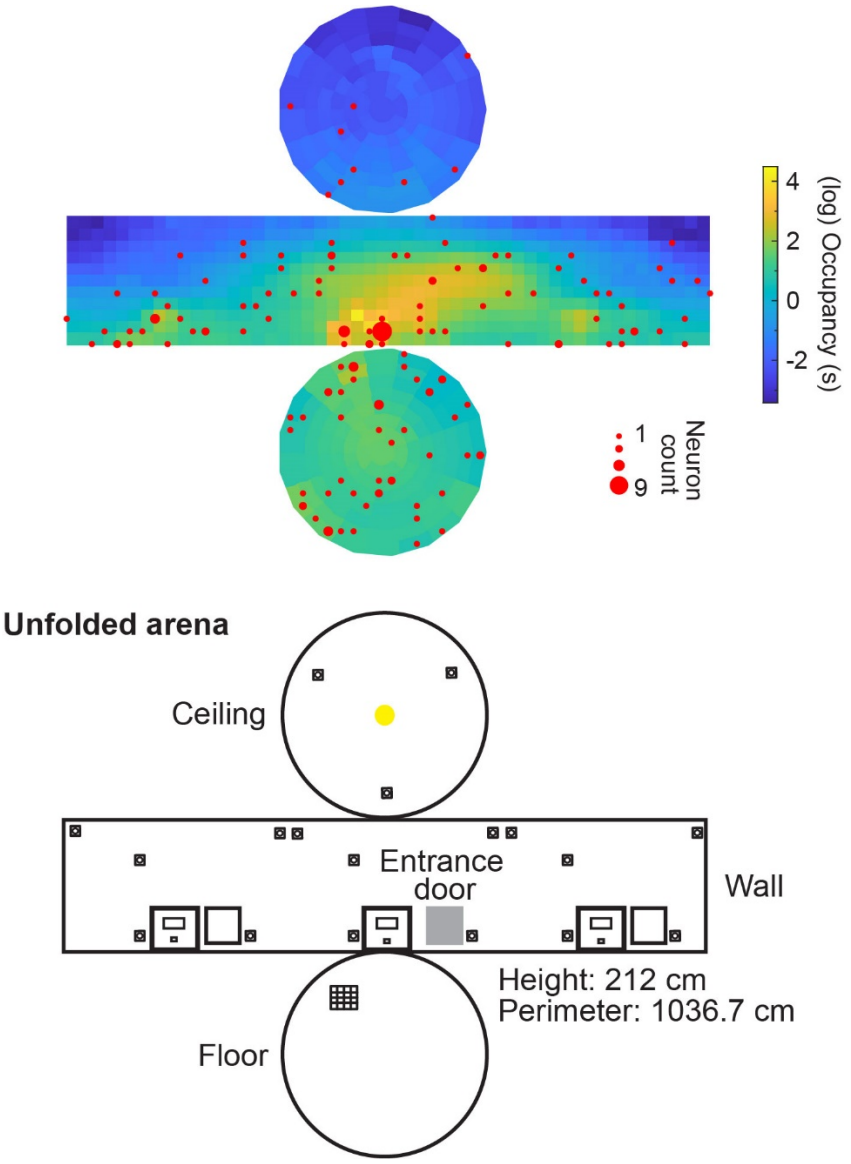

Fig. S9. Top, preferred firing fields (red dots) for all Facing Location (FL) cells superimposed on the average occupancy color map (unfolded 2D map) across monkeys. Bottom, unfolded 2D arena map (same as Fig. S1B).

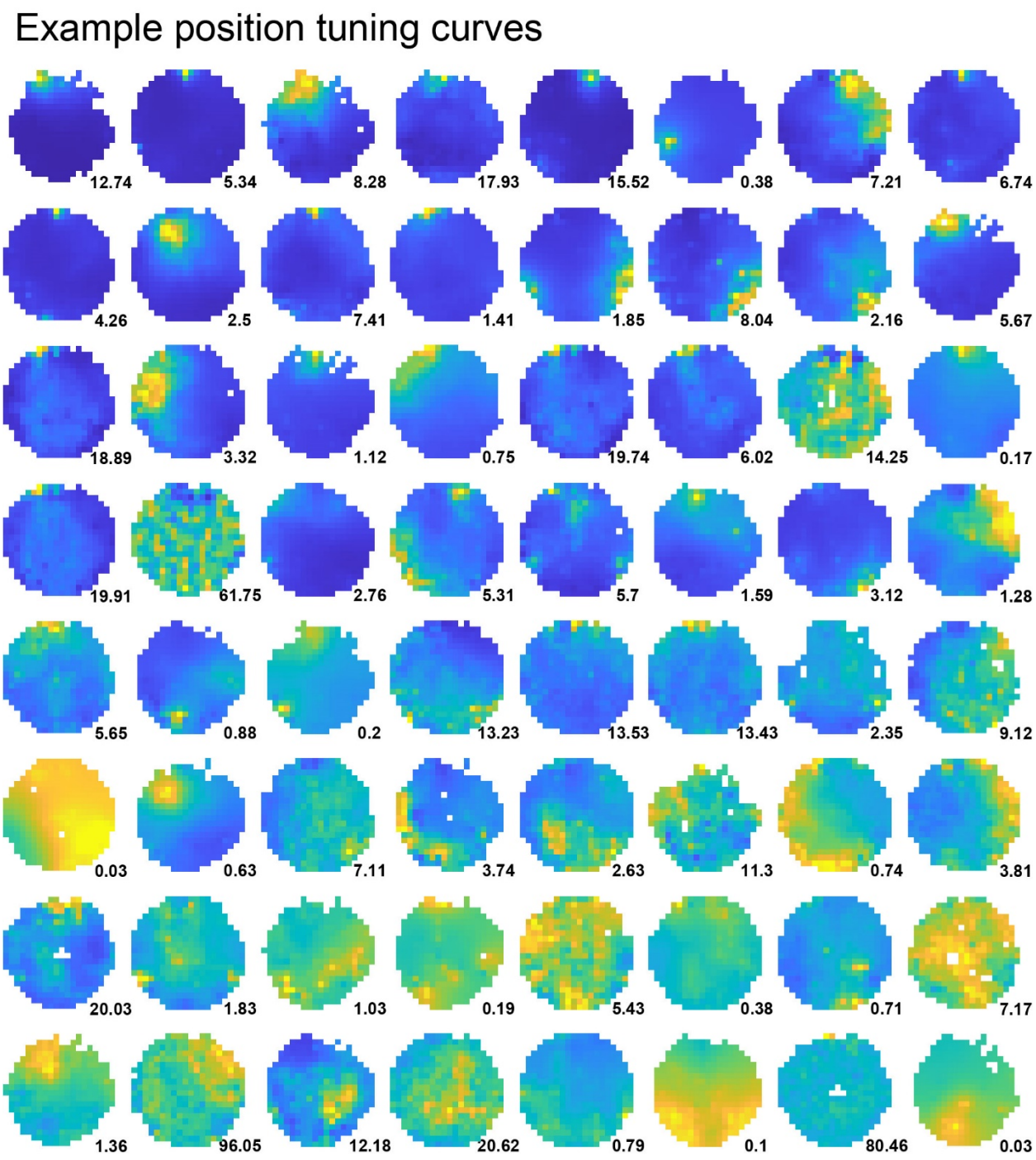

Fig. S10. Example position tuning curves (model-based) for 64 neurons that significantly encode position. Peak firing rate is indicated at bottom right for each neuron. Neurons were sorted by how well position predicts firing, from left to right, top to bottom.

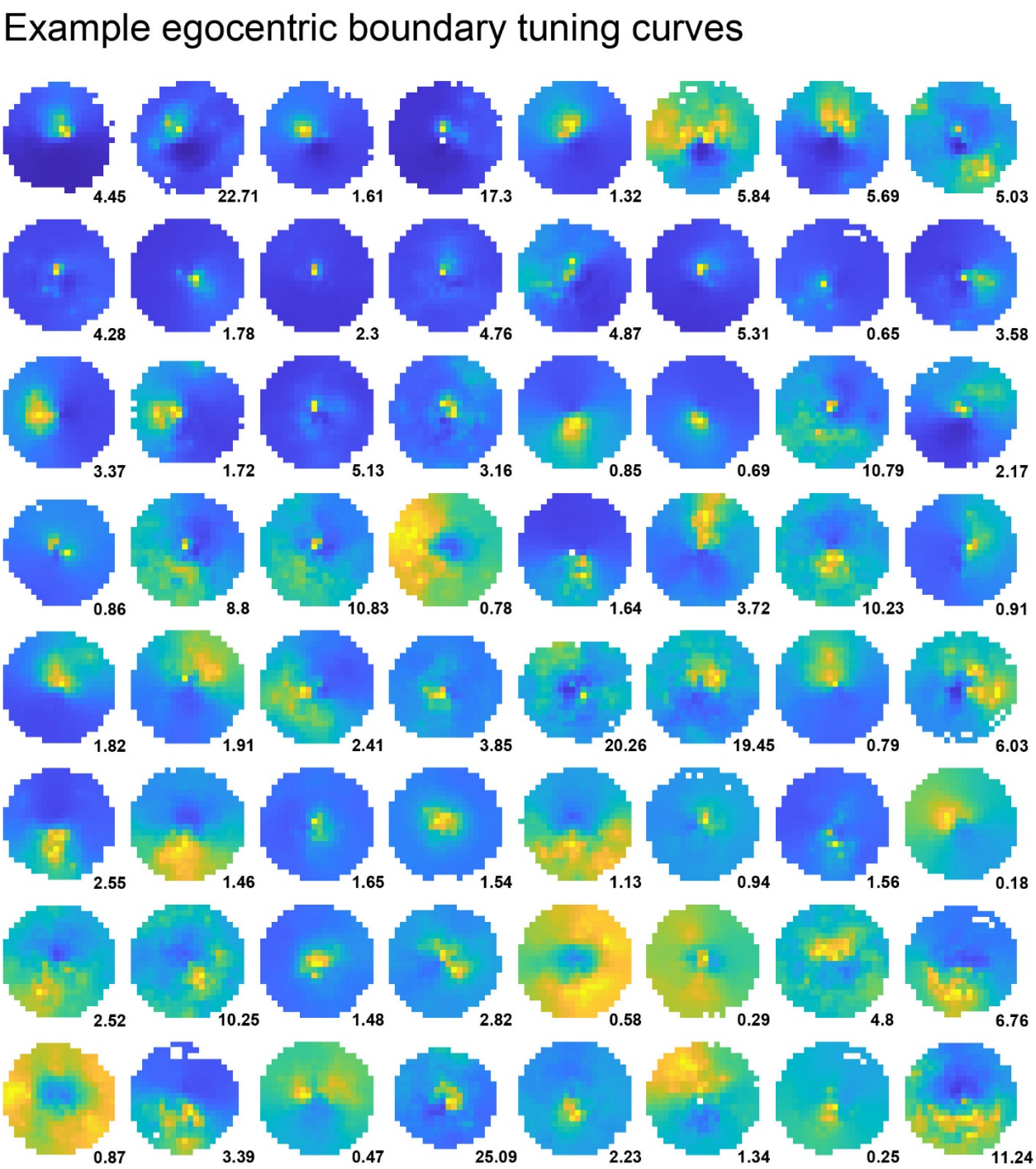

Fig. S11. Example egocentric boundary tuning curves (model-based) for 64 neurons that significantly encode egocentric boundary. Peak firing rate is indicated at bottom right for each neuron. Neurons were sorted by how well egocentric boundary predicts firing, from left to right, top to bottom.

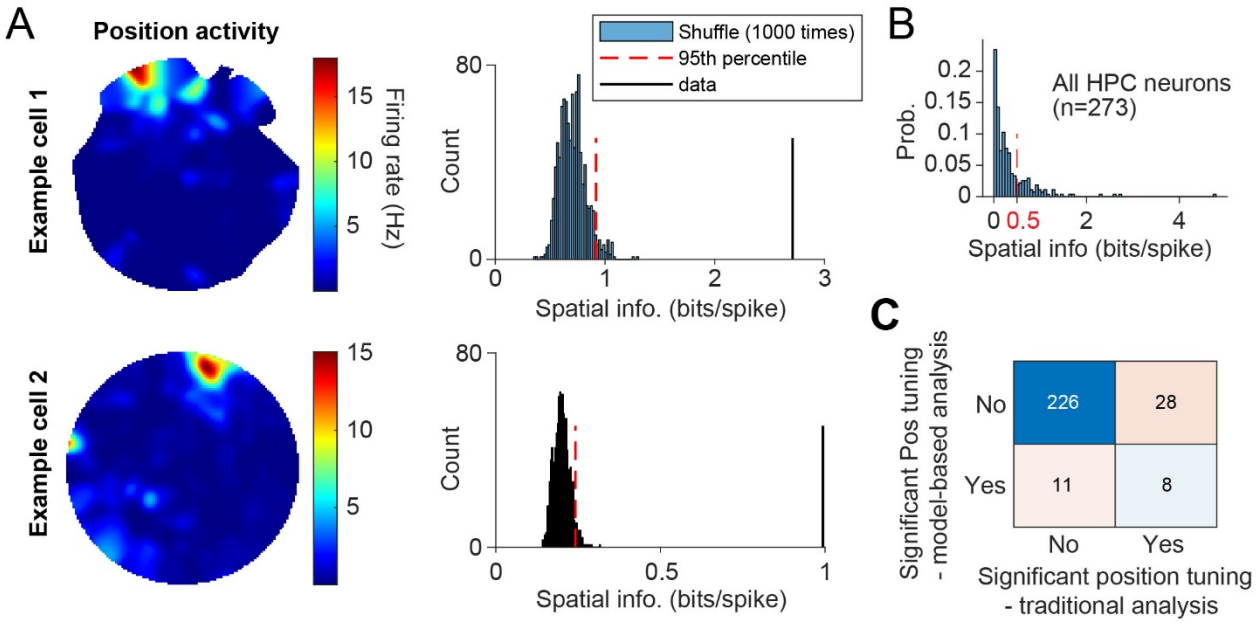

Fig. S12. Position tuning analysis using traditional methods. (A) Left, position activity color map for 2 example neurons. Right, spatial information for the actual data (black line) and shuffled distribution (histogram, 1000 times). Red line indicates the 95th percentile of the shuffled distribution**. (B)** Histogram of the distribution of the actual spatial information for all HPC neurons. A neuron was considered spatially-tuned if the actual spatial information is larger than 0.5 and is larger than the 95th percentile of the shuffled distribution. **(C)** Confusion chart for the number of neurons showing position tuning using model-based analysis and traditional analysis.

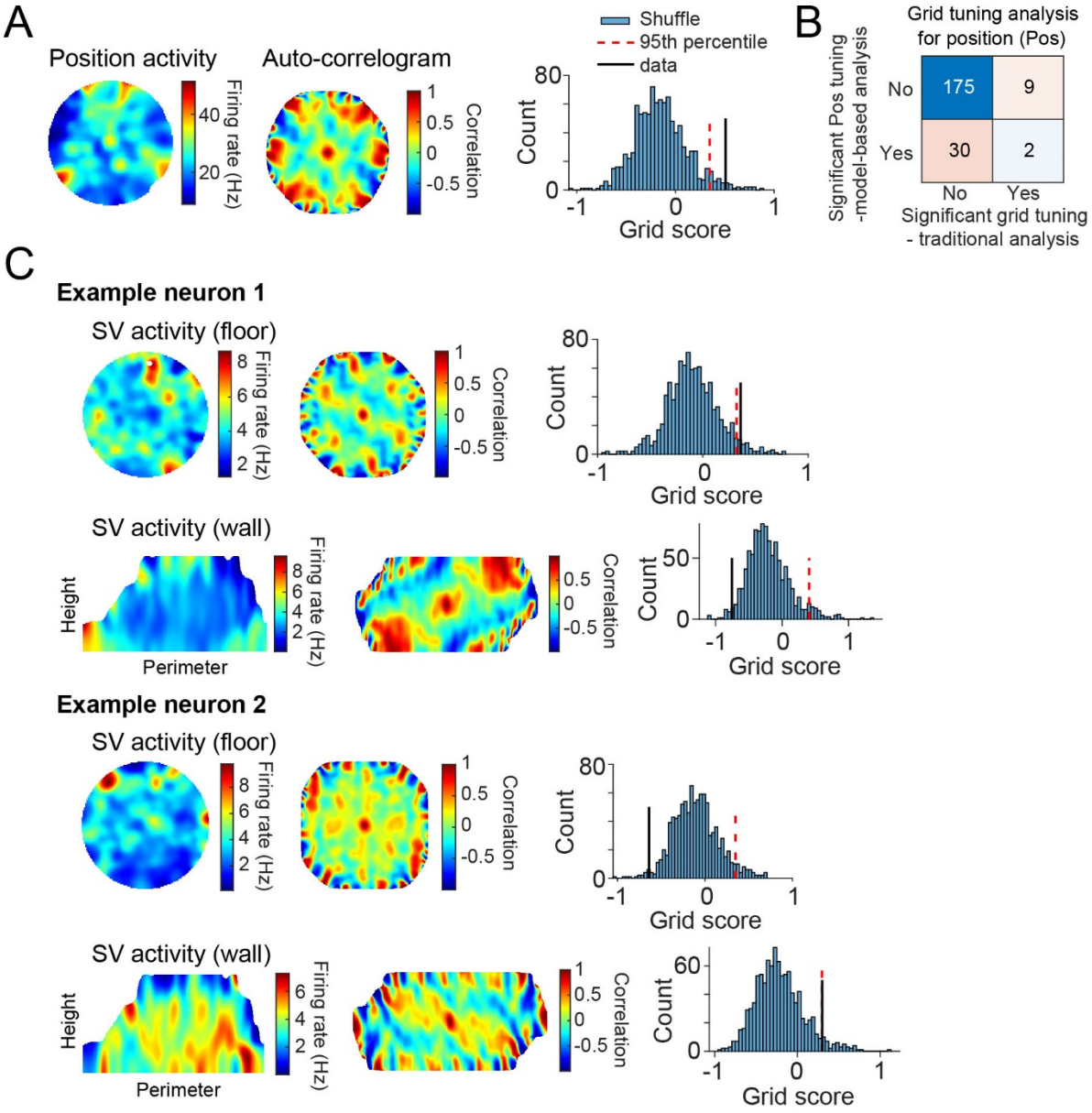

Fig. S13. Grid tuning analysis for position and spatial view using traditional grid score-based analysis. **(A)** Position activity color map (left), auto-correlogram (middle), and grid score histogram (right, 1000 times shuffling) for one example EC neuron. Right: A neuron was considered significantly grid-tuned if the actual grid score (black line) is larger than the 95th percentile (red dashed line) of the shuffled distribution. **(B)** Confusion chart for the number of neurons showing position tuning and grid tuning using model-based analysis and traditional grid tuning analysis. **(C)** Similar to **(A)** but for spatial view (SV) activity (on the floor and wall) for 2 example EC neurons from monkey K. Example neuron 1 shows significant grid tuning for SV activity on the floor but not on the wall; example neuron 2 shows significant grid tuning for SV activity on the wall but not on the floor. Overall, 9% (4/46) neurons showed significant grid tuning either on the floor or on the wall.

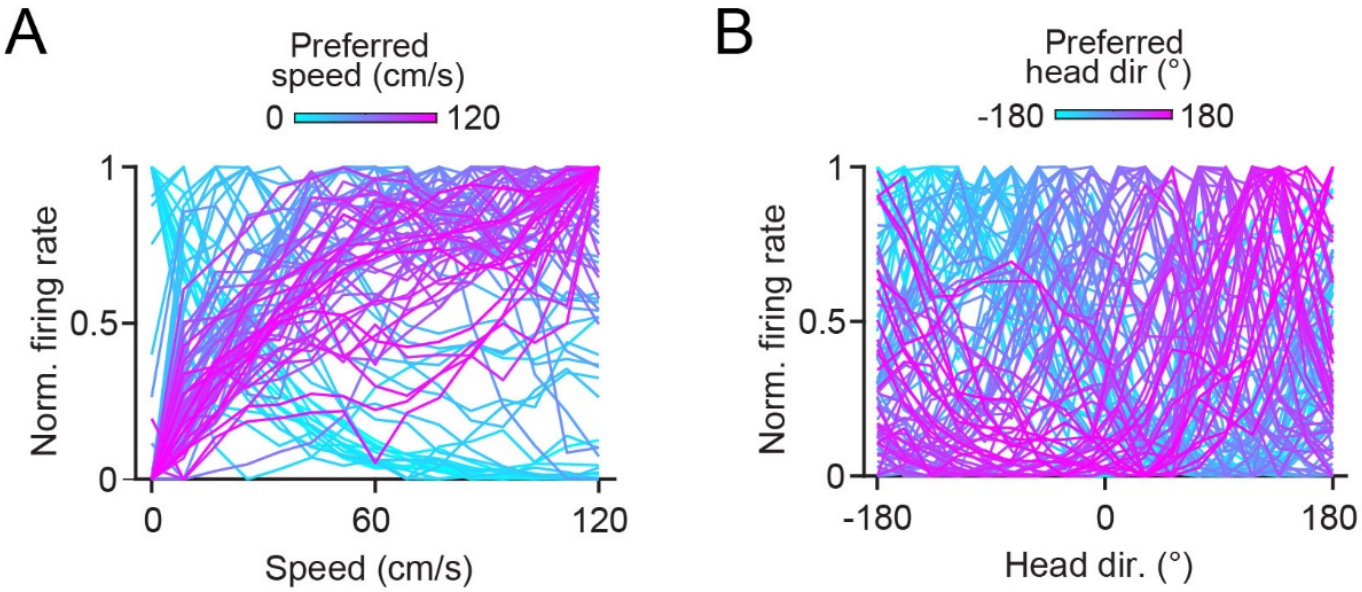

Fig. S14. Normalized speed tuning curves (A) and head direction tuning curves (B) for all significantly tuned neurons. Tuning curves are color coded by their preferred speed or head direction.

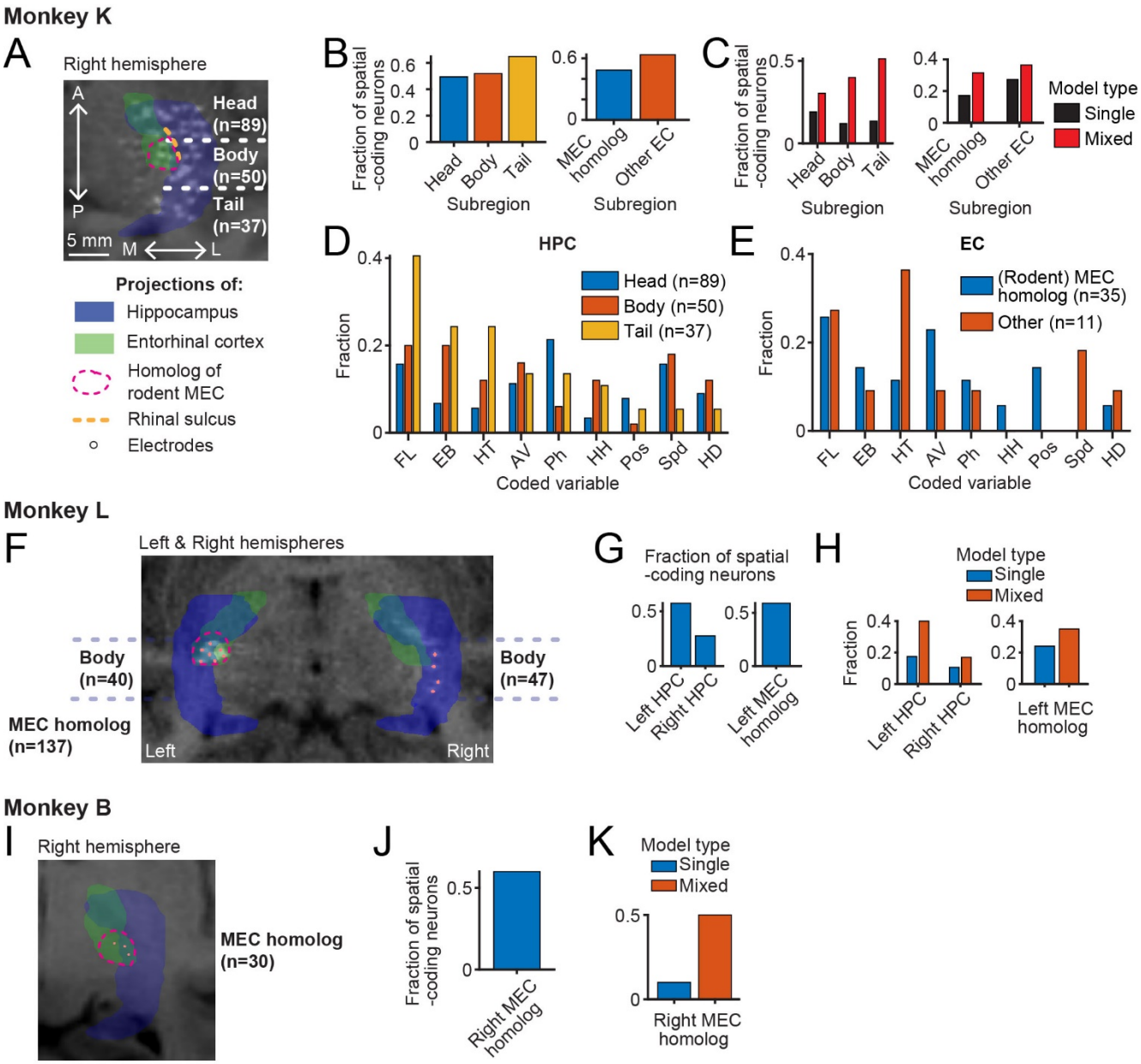

Fig. S15. Anatomical distribution of spatial coding in macaque hippocampal formation. (A-E) Data for monkey K. (A) Top view of hippocampus (blue) and entorhinal cortex (green), as seen in MRI images. White marks (as seen in MRI-aligned CT images) correspond to electrodes. Dashed magenta line encompasses the approximate area homologous to rodent medial entorhinal cortex (MEC). Dashed gray line indicates the rhinal sulcus. Horizontal dashed lines indicate the boundaries used to separate the hippocampus into head, body, and tail subregions. **(B)** Fraction of spatial-coding neurons in different hippocampus (head: 49%, body: 52%, tail: 65%) and entorhinal cortex subregions. **(C)** Fraction of neurons that encode a single or multiple ('mixed') variables for different subregions (single vs. mixed selectivity, head: 19% vs. 30%, body: 12% vs. 40%, tail: 14% vs. 51%). **(D)** and **(E)** Fraction of neurons that encode each variable in the hippocampus and the entorhinal cortex subregions. **(F-H)** Data for monkey L (left and right hemispheres). Pink dots indicate electrodes locations. **(I-K)** Data for monkey B (right hemisphere only).

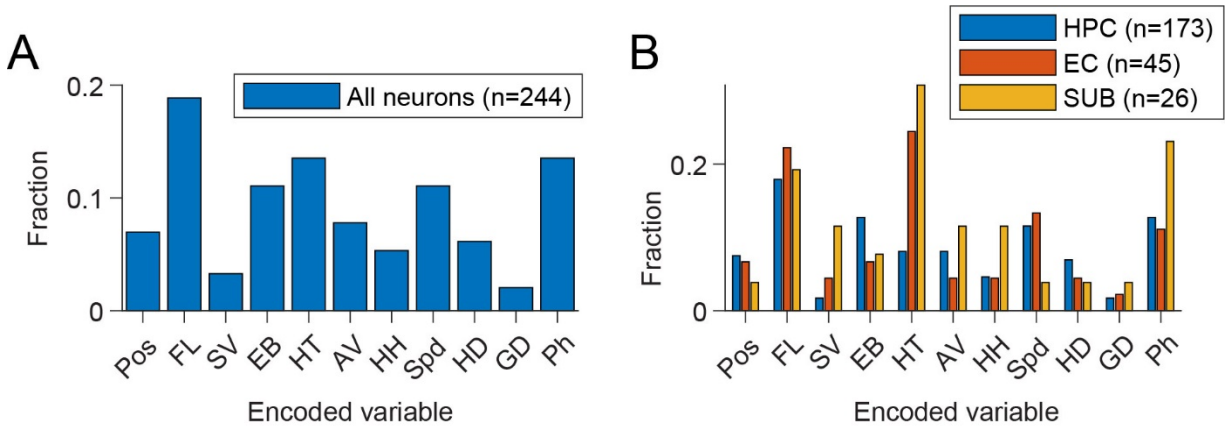

Fig. S16. Comparison of eye and head tuning (animal K only). (A) Bar plot showing the overall fraction of neurons encoding each variable when fitting all head and gaze properties simultaneously. **(B)** Breakdown of **(A)** into individual regions.

Hemisphere	Region	Monkey		
		B	K	L
Left	HPC		10	40
	EC		3	137
	SUB		1	83
Right	HPC		176	47
	EC	30	46	
	SUB		26	
Sessions		13	37	86

Table S1. Breakdown of recorded neurons across regions, hemispheres, and monkeys.